KEM-49

InSAR subsidence data for salt cavern management in Twente

Final Report

30-03-2026

SENSAR

TNO innovation for life

This is the final report for the KEM-49 project, financed by the Ministry of Climate and Green Growth.

Project team:

Reinier Oost	Sensar B.V.
Corné Verhoeven	Sensar B.V.
Joana Eenhoorn	Sensar B.V
Peter Fokker	TNO – Energy & Materials Transition
Suresh Palanisamy Vadivel	TNO – Energy & Materials Transition
Darren Jones	TNO – Energy & Materials Transition

Table of Contents

Glossary

AHN	Actueel Hoogtebestand Nederland
asc	ascending
APS	Atmospheric Phase Screen
BJP	Bekendam-Jakob-Pinkse
DS	Distributed Scatterers
dsc	descending
FLAC	Fast Lagrangian Analysis of Continua
InSAR	Interferometric Synthetic Aperture Radar
KGG	Ministry of Climate Policy and Green Growth
KEM	Kennisprogramma Effecten Mijnbouw
LOS	Line Of Sight
PS	Persistent Scatterers
PSI	Persistent Scatterer Interferometry
SNR	Signal-to-Noise Ratio

1. Project Background

Salt mining has taken place in the Twente region for more than 60 years. It has been exploited at a relatively shallow level, resulting in subsidence at surface level and one sinkhole event. In this region tens of caverns have been identified as being potentially unstable. For this reason, a monitoring plan has been implemented, using a micro-seismic network and sonar measurements.

In order to improve the assessment of cavern stability, the Ministry of Climate Policy and Green Growth (KGG) is looking for additional monitoring methods. Interferometric Synthetic Aperture Radar (InSAR) is such a potential monitoring method. InSAR is strong in measuring small elevation changes (mm-level) over large areas with a relatively high measurement frequency. Therefore, these measurements can potentially be used to identify salt caverns that are unstable and therefore prone to more subsidence and sinkhole development, and require infilling. An improved understanding of the cavern deformation in relationship to the surface deformation could facilitate a better risk assessment and mitigation procedure.

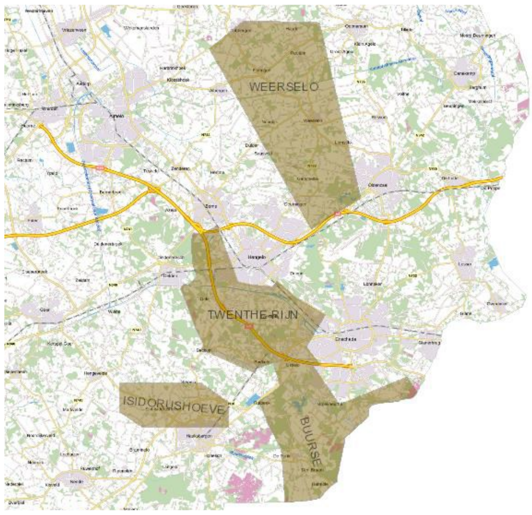

Figure 1. The area of interest for this study as provided by the client; all current salt cavern sites in the Twente region, operated by Nobian.

As part of the KEM-49 project, we have investigated the potential of using InSAR measurements for the detection of salt cavern instability. The Twente-Rijn area (Figure 1) served as a pilot area for the analysis.

1.1 Research Questions

The project focused on answering the following research questions:

1. What are the quality control procedures of the InSAR data and what levels of accuracy and precision can be expected?
2. What are the global experiences with salt cavern monitoring using InSAR?
3. Which locations over the last 10 years show subsidence rates which correspond to possible unstable salt caverns in Twente?
4. What is the coupling between (known) Twente cavern deformation and subsidence data? Which Twente caverns may be unstable?

In this report we are answering these research question and provide a conclusion.

2. Literature review on cavern instability & InSAR monitoring

In the following sections we summarize relevant research done with regards to salt cavern instability and InSAR monitoring, answering research question 2: What are the global experiences with salt cavern monitoring using InSAR?

2.1 Monitoring of salt caverns with InSAR

Ground motion monitoring with satellite-borne InSAR has become a mature technology since the launch of the first satellites in 1992 (Hanssen, 2001) and (Ferretti, 2014). The currently most popular InSAR service is provided by ESA with the Sentinel-1 satellites from the European Ground Motion Service Torres et al (2012). It is easy to find publications that address the ground motion above salt caverns. We list a few.

A study focusing on sinkholes was performed by Rucker et al (2013). They show that subsidence monitoring with InSAR is a useful tool; however, they have not seen signs of additional subsidence prior to sinkhole formation. This may be related to the fact that they used only two interferograms (three images), which were taken from the old Envisat satellite mission, and no removal of the atmospheric signal was performed. Malinowska et al (2018) also present a field case, on a field with quite shallow salt caverns. They show the effectiveness of using InSAR for monitoring. InSAR monitoring allows to identify the areas with the largest dynamics of surface movement, even in regions where classical surveying had not been conducted. They used more recent Sentinel images, but neither here was the atmospheric signal removed. Sufficient coherence was achieved thanks to the urban area, however, a great improvement would have been possible when many images would have been used in a workflow with Persistent Scatter Interferometry. Liu et al (2019) deliver a study in which they combine InSAR data with levelling data, and show their consistency. They also provide a connection to the salt production data and the temperature: larger temperatures enhance the salt dissolution rate and the associated subsidence velocity. No geophysical modelling is provided. A similar study was performed by Parwata et al (2020) on a cavern field in Bosnia and Herzegovina. They demonstrate how the InSAR can be used to map the spatial distribution of ground movement, and show how the patterns have developed with the creation of new caverns and shut-in of older ones. They convincingly demonstrate the power of using many images (over 200) in a PS-InSAR workflow. A deeper set of caverns (1400-1800 m) is addressed by Montalti et al (2023) also with the intent to demonstrate the utility of InSAR for monitoring. They show how such monitoring can enable storage facility operators to understand the deformation phenomena, but also how it can contribute to enhanced withdrawal and injection rates. Fibbi et al (2025) present salt caverns in the context of underground gas storage. They show how the type of storage affects the surface deformation, for which both vertical and East-West horizontal movements can be estimated with InSAR. With storage in a depleted gas reservoir, seasonal subsidence and uplift occurs with the depletion and pressurization of the pore space, while in salt caverns the subsidence continues – only at a different pace depending on the pressure in it.

A common feature of publications like the ones just mentioned is that InSAR is a powerful tool for ground movement monitoring above salt caverns that change in volume. A great characteristic of InSAR is that historical data can often be acquired, even when no problems had been expected and no monitoring had been put in place beforehand. The behaviour prior to and during incidents can thus be studied in hindsight, even when they had not been anticipated. When enough scatterers are available, InSAR is a great tool to map the spatial and temporal deformation patterns.

An important point that these studies demonstrate is that there is no such thing as 'standard InSAR'. The articles demonstrate a vast range in the quality levels of the InSAR results. Single or few interferograms in an SBAS workflow give far smaller accuracy and time-resolved information than studies with a PSI workflow and many interferograms. The source data and the methodology thus are important aspects, especially in relation to the quality level that one would like to achieve.

Another point of concern is the link between surface movement estimates and the subsurface geophysical behaviour. The drawback of many of these studies is that the physical understanding of the subsurface behaviour is limited, and not connected to the surface deformation. There are fewer studies that address this coupling.

2.2 Coupling of monitoring results with geophysical modelling

The use of data to constrain model parameters has a long history in geophysics. Standard textbooks are those of Menke (2018) and Tarantola (2005). Such inverse modelling has also been deployed when the data are InSAR-derived surface movement data (Fokker et al, 2025). Examples are subsidence due to fracture development during injection of CO_2 (Vasco, 2010); hydrocarbon production (Janna et al, 2012, Fokker et al, 2016); groundwater extraction (Yan & Burbey, 2008); geothermal energy production (Wang et al, 2024); or combinations of several phenomena (Verberne et al, 2025). The parameterization can be anything between the endmembers of simple linear forward models with a few parameters and complex numerical model chains with spatially distributed characteristics. The associated inverse scheme can range from straightforward linear inversion to complicated MCMC methods or ensemble-based data assimilation techniques.

The use of inverse modelling with subsidence estimates is not commonly applied. This is also the case when addressing surface movement above salt caverns. Still, some work has been performed in this direction. Even et al (2020) studied displacements above the storage cavern field at Epe in Germany. Many caverns are present here, at around 1000 m depth, for the storage of natural gas and oil. They used InSAR to derive vertical and horizontal East-West movements. Indicative for the lack of standardization is that although the researchers made use of a widely accepted InSAR-processing tool (StaMPS), they still had to implement many workarounds for their use-case. The movements observed are analysed in the context of the pressure in the caverns as the driving force for cavern squeeze, and a Multi-Mogi model for the translation of the volume loss to the surface (Mogi, 1958). A reasonable correspondence between InSAR and ground truth was obtained, but some systematic deviations persist. The analysis of the movements give good correspondence with the vertical movements of the Mogi sources, but an unsatisfactory fit of the horizontal movements. The Mogi sources seem to have a too large range of influence for the horizontal movements.

A similar study was performed by Gao et al (2025). They analysed a salt production site in China where subsidence reached up to almost 40 mm / year. An inverse modelling with Mogi sources was deployed to estimate the annual volume loss in the region. The inverse analysis was not constrained by prior data, only by a smoothness requirement.

Furst et al (2021) studied a field of deep caverns (around 2000 m depth) in Vaufert, France. They also used vertical and horizontal movements. Horizontal movements in the North-South direction were inferred from the East-West movement in combination with an assumption of radial symmetry around the centre of the subsidence bowl. Then they performed an interpretation with 4 different forward model constellations: (i) a single Mogi source; (ii) a 2D plane with a dislocation according to Okada's theory (Okada, 1992), and (iii), (iv) a distribution of 21 or 28 Okada dislocation planes. However, the areal distribution of the dislocation planes reaches much further than the physical dimensions of the salt caverns. The physical dimensions background of this choice seems questionable.

Models different from the Mogi nucleus of strain have also been employed. Fokker and Kruse (2002) use a Gaussian function to describe surface movement measurements. These type of functions have also been used in longwall mining, and some authors have elaborated on them (e.g. Tajduś et al, 2021)However, the Gaussian functions lack a physics basis and their decay towards larger distances is commonly too strong: the range of influence of real cases is larger than the estimates by these models. A study on different influence functions was performed by Fokker and Osinga (2018). They showed that the correct influence function is critically connected to the geometry of the centre of compression: a salt cavern with a large height / radius ratio is better represented by a combination of horizontal double forces. The use of suboptimal influence functions may presumably be the cause of the mismatches observed by Even et al (2020) and Furst (2021).

A last comment in this section concerns the use of vertical and horizontal movements in inverse modelling. Most studies perform a disentanglement of horizontal and vertical movement from the movement estimates along the Line Of Sight (LOS) before going into further interpretation. This additional interpretation step, however, is a possible source of data loss and error. Firstly, only the period in which ascending and descending data are both available can be used. Secondly, interpolation or Kriging needs to be performed prior to combination of the two satellite geometries. Interpolation should be avoided if possible; it always brings the risk of creating artefacts or loosing accuracy. And thirdly, when the ascending and descending directions are not precisely opposite with a 180° angle, the vertical movement can not be derived exactly. The usual approximation that N-S movements contribute only marginally to the LOS movements may well be inadequate on the northern and southern flanks of the subsidence bowl. An example of this is shown in Even et al (2020) (Figure 10 in their paper). We therefore advocate to use the LOS data directly in the inversion exercise. Indeed, a geophysical model calculates a 3D movement vector, which can then be projected on the LOS directions which are present (Fokker et al, 2016). In all cases, inversion or data assimilation is required to account for the uncertainty in all parts of the model and model parameters. A stochastic approach is often the preferred way to go (Fokker et al, 2025).

2.3 Unstable shallow salt caverns

A good introduction to salt solution mining is provided by Groenenberg et al (2025). It is a practical guide to get acquainted with many aspects of salt mining – with some attention to the shallow salt caverns in the Hengelo area as well. Another recent text is the one by Yang & Wang (2024). They focus on caverns used for gas storage, and also give some attention to monitoring with InSAR.

A quite early publication focusing on incidents with underground salt caverns is the one by Bérest and Brouard (2003). While they claim that underground storage is the safest way of hydrocarbon storage, incidents can still happen. They provide descriptions of field cases in which 4 types of incidents happened. The first are blowouts, related to a mismatch in the fluid balance. The second are mechanical instabilities of the cavern, leading to leakage. These may have to do with the pressure distribution of the various fluids, the geological environment, or the quality of the well completions. The third is cavern instability. This may lead to subsidence – slow or sudden; with a smooth subsidence bowl or a sharp sinkhole. Instability may be connected to salt creep or to the failure of a cavern roof. In all cases, the mechanical behaviour of salt is key knowledge. The last one is connected to cavern abandonment. An abandoned, sealed cavern may continue to develop in temperature, size, and associated pressure. Large pressures may cause fracturing of the cavern roof or an increase of the permeability of the fracture wall. Quality governance is required to regulate cavern abandonment, as the development of risks may continue for many years.

Yang et al (2013) give a more in-depth analysis of the major risks associated with storage in salt caverns, with an elaborate fault tree analysis. While they see leakage as the largest risk, they also address ground subsidence and cavern failure. For subsidence, they describe 5 cases and identify the underlying as risk factors:

- The rocksalt creep characteristics (causing excessive shrinkage and volume loss)
- Cap rock properties and thickness (causing possible failure)
- Height/diameter ratio of the cavern (relating to geometry of plasticity near the cavern)
- Difference between cavern pressure and stress (the driving force behind salt creep).

Cavern failure might be caused by excessive cavern shrinkage, by cavern collapse, or by cap rock failure. The authors describe 6 cases and identify partially the same risk factors as with the subsidence risk:

- Cap rock properties and voids in the cap rock
- Faults near the cavern (natural channel for leakage; and for failure by activation)
- The rocksalt creep characteristics and strength
- Non-uniform stresses

Bérest (2017) further investigated the occurrence of craters above salt caverns. Twelve cases were assessed, with two mechanisms identified: piston-like displacements creating a sharp-edged sinkhole, and hourglass-like phenomena creating more smooth depressions. The criterion for a piston-like failure to occur is related to the friction between the column that is falling down and the surrounding rock: this friction must be overcome by the weight of the column. This translates to a critical ratio between radius and height of the column falling down, R/H. Clearly, the height is the depth to the top of the cavern. As a rule of thumb, sinkholes are not expected above a cavern whose R/H ratio is much smaller than 1/3. Criteria for hourglass-like failures are harder to give – but an important attribute is the bulking factor: the increase in volume of material that has failed. For caverns that are deep enough, the bulking factor will prevent the failure to reach the surface. Sinkholes will not develop when the failed material is enough to fill the volume that is available in the column between the bottom of the cavern and the surface.

In a later publication, leakages were studied (Bérest et al, 2019). With 11 cases, the most important attributes were identified that can help to prevent leakages or discover them early enough to be able to repair them. These attributes are the well completion quality, the pressure monitoring, and mechanical integrity tests.

The thesis of Eising (2021) aimed at bringing together all known incidents in caverns which are used for storage. The size of the inventory allows to make general comments. When discriminated against depth, the largest risks are connected to shallow caverns (less than 500 m depth). With regard to the type of salt body in which the caverns are created, he concludes that salt domes are most risky.

Much of the work described, and more, has been brought together in a large literature review that is part of the study by Bérest et al (2023). The study is targeted at the use of caverns for storage of hydrogen, but brings together all knowledge that is relevant: a comprehensive literature review summarizes the insights obtained from accidents and near-accidents in underground storage projects in conglomerates of salt caverns worldwide. With regard to leaks, we learn that an important feature is the cavern and well design. A single barrier is not safe enough. For an incident to proceed, cavern breach is accompanied by a pathway from the cavern to the outlet – and cases have been documented in which this resulted in blowouts, sinkholes, and explosions. For subsidence risks, case histories of caverns at different depths are described. A notion to remember is that the volume loss of a cavern is not always completely propagated to the volume loss of a subsidence bowl. For cratering, an important observation is that it has never been observed above caverns deeper than 500 m below the surface.

2.4 Concluding remarks

A lot of knowledge is available on the behaviour of salt caverns and the possibility of incidents leading to failure. The deformation of caverns is often slow, associated to the creep of the rocksalt. Sometimes the deformation is sudden, and associated to incidents. The resulting spatial distribution of the deformation can also be gradual or abrupt, like in sinkholes. Information about cavern position and their expected behaviour is important when assessing risk of incidents happening.

The monitoring of failures with time-resolved InSAR is not common. Even less common is the linkage between monitored surface deformation and physical modelling of the failure phenomena. Some studies have employed inverse modelling to do so; however they mainly targeted slow and smooth deformation signals. To bring this knowledge position further, it is necessary to deploy models that mimic catastrophic failure and calculate the consequences in terms of surface movements.

3. Methodology

The following sections provide an overview of the methodology used. We separate the InSAR processing procedure and quality control and the geomechanical modelling to determine the subsidence profile for the caverns.

3.1 Interferometric Synthetic Aperture Radar (InSAR)

In the following sections we provide an overview of the InSAR processing steps and quality control procedure, answering research question 1: What are the quality control procedures of the InSAR data and what levels of accuracy and precision can be expected?

Interferometric Synthetic Aperture Radar (InSAR) enables the detection and quantification of surface deformation with millimetre-level precision across infrastructure, the built environment, and the subsurface. The technique is particularly effective for monitoring vertical displacements—such as land subsidence—but can also capture horizontal movements in specific contexts, for example in the case of quay walls or other laterally unstable structures. InSAR measurements are derived from repeated acquisitions of radar signals collected by Earth-orbiting satellites, which travel at velocities of approximately 8 $km\,s^{-1}$ at altitudes typically between 500 and 800 km. Depending on satellite revisit cycles and mission configurations, it is possible to obtain up to 60 observations per year for a given location. These observations can cover extensive spatial areas (greater than 100 km^2) and yield exceptionally high point densities—up to 100,000 measurement points per km^2, contingent on the sensor's spatial resolution.

Radar imaging is largely unaffected by meteorological conditions or illumination, enabling data acquisition independent of weather or time of day. In SAR systems, the satellite emits microwave pulses and records the backscattered signal, a process conceptually similar to echolocation. The transmitted signal is reflected by the ground, buildings, and other surface features, with man-made structures possessing sharp edges or strong geometric contrasts producing the strongest returns. As a result, InSAR is particularly effective in urban settings, where stable reflectors are abundant. Both the phase and amplitude of the received signal are measured, providing information on signal strength as well as the path length between the satellite and the reflecting surfaces.

The InSAR technique exploits the radar wavelength (λ) to infer millimetre-scale surface displacements, functioning in principle as a highly precise measurement standard. This is achieved by analysing the phase component of the returned radar signal. The phase represents the fractional position of the wave cycle relative to a reference oscillator at the moment the signal is received by the satellite. Because the satellite records the phase during each acquisition, phase values from different

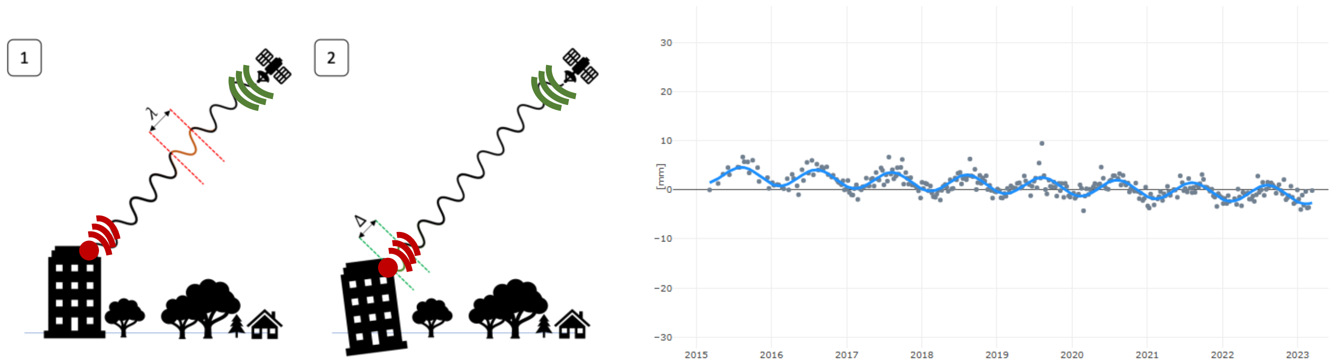

Figure 2. Left: [1] the first situation and [2] the second situation where the house has moved and we capture a phase difference in the signal (Δ). Right: An example of a timeseries produced with InSAR. The blue line gives the model fit based on the individual measurements in time.

observation times can be compared. Any displacement of an object alters the path length travelled by the radar signal, which manifests as a measurable phase difference between successive radar images (Figure 2, left). By relating this phase difference to the known wavelength of the radar signal, the corresponding deformation can be quantitatively determined.

3.1.1 InSAR processing chains

InSAR does not denote a single, standardised procedure; rather, it serves as an umbrella term encompassing a suite of techniques that exploit the phase information contained in radar observations. Although InSAR methods are most commonly associated with measuring surface deformation, they can also be employed to derive topographic information and to characterise atmospheric delays that affect radar signal propagation.

For InSAR processing in temperate regions with substantial infrastructure, Persistent Scatterer Interferometry (PSI) represents the most suitable approach for obtaining highly accurate and precise deformation measurements. The fundamental principle of PSI is the identification and utilisation of dominant radar scatterers that exhibit long-term temporal stability, referred to as Persistent Scatterers (PS). These targets typically display low phase noise and therefore provide reliable measurements for estimating surface deformation. Conventional PSI workflows construct a network of PS points to derive double-differenced phase observations, followed by temporal modelling and network adjustment procedures to estimate both deformation time series and precise geolocation for each PS. This methodology allows most PSI implementations to operate at the full spatial resolution of the satellite imagery, making them particularly well-suited for infrastructural environments where deformation patterns are spatially discrete and fine-grained. The geolocation step further enables accurate spatial positioning of the PS within the built environment. The typical output of a PSI workflow is a high-density point cloud of PS measurements. Because the technique relies on long temporal sequences to identify consistent deformation trends and ensure robust phase-to-displacement conversion, PSI is especially effective for detecting subtle, gradual deformation processes that are otherwise imperceptible to the human eye. An example of an InSAR time series is illustrated in Figure 2 (right).

Following the PSI workflow, the resulting deformation estimates must be geodetically calibrated to ensure proper spatial and vertical referencing. The choice of an appropriate reference datum depends on the application. A reference can be established statistically by identifying a locally or regionally stable area or by linking the PSI results to independent in-situ measurements, such as GNSS or levelling benchmarks. The measured surface subsidence represents the cumulative effect of deformation processes occurring at different depths, meaning that signals from multiple subsurface mechanisms are superimposed. In general, deeper deformation sources tend to produce subsidence patterns with a broader spatial extent, whereas shallow processes generate more localised signals. For applications requiring comparison with external geophysical or environmental datasets - such as sea-level rise or groundwater dynamics - calibration to an absolute datum is essential. Conversely, studies focusing on shallow, site-specific deformation often benefit from adopting a local or regional datum, which enhances the visibility of near-surface processes.

The main steps in the InSAR processing chain applied in this project are visualized in Figure 3 and include:

- **Pre-processing**: During this step, satellite images are aligned with one another (coregistration).
- **PSI-processing**: In PSI processing, deformation time series are produced based on the complex SAR imagery.
- **Geodetic processing**: Raw PSI-results require geodetic calibration to ensure proper referencing.

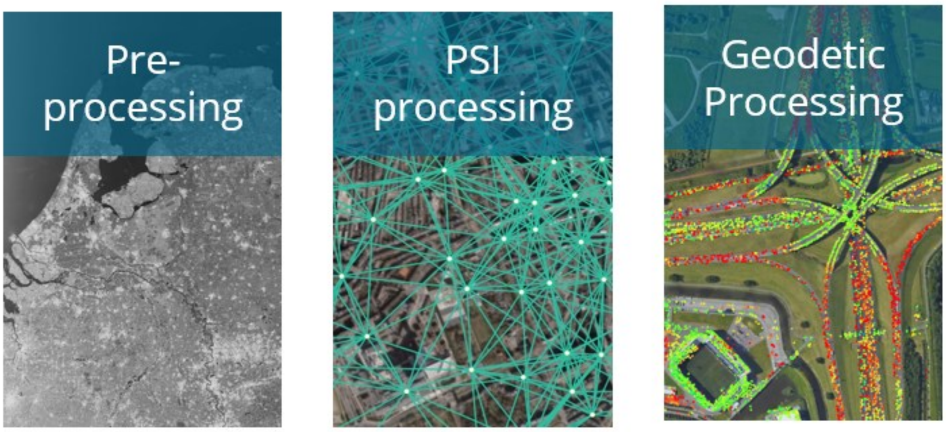

Figure 3. The InSAR data processing chain.

3.1.2 Precision, accuracy, reliability and coverage

Precision is primarily influenced by stochastic (random) noise, whereas accuracy is governed by systematic errors or biases. Figure 4 visualised the difference between precision and accuracy.

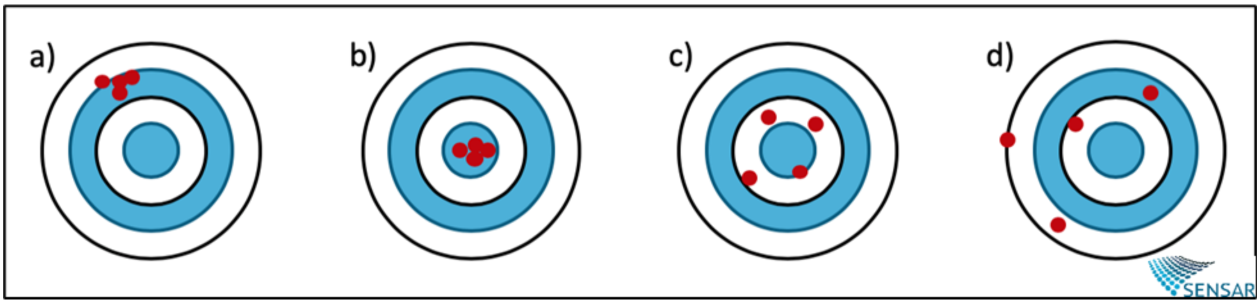

Figure 4. a) precise b) accurate and precise c) accurate d) not accurate and not precise.

In PSI workflows, the achievable **precision** is largely determined by, and proportional to, the radar wavelength. A commonly applied rule of thumb is that Persistent Scatterer (PS) points should exhibit phase noise levels below approximately 10% of the wavelength to ensure reliable deformation estimates. Because PSI techniques rely extensively on temporal regression models to interpret phase observations, precision is often expressed in terms of the estimated uncertainty of the linear subsidence rate rather than the noise of individual phase measurements. This focus on the temporal domain reflects the method's dependence on long, coherent time series for deriving robust deformation trends. As can be seen in Figure 5 the theoretical accuracy of the linear trend is within 1 mm/yr for Sentinel-1 in about 2-years.

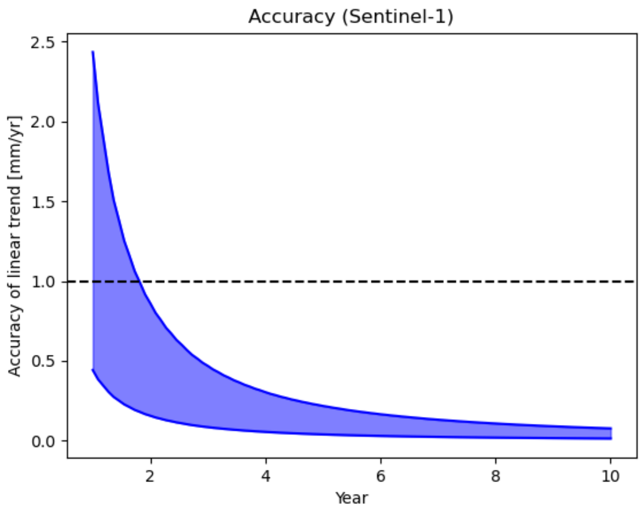

Figure 5. Theoretical error propagation of the accuracy of the estimated linear trend using 6-day Sentinel-1 observations. The upper limit is for measurements with lowest quality, the lower limit for measurements with best quality.

The achieved **accuracy** of PSI-derived deformation estimates is largely determined by the geodetic calibration procedure and can only be quantified through an independent geodetic validation study. Regardless of whether the calibration is based on statistical region-selection or on direct linkage to external reference measurements, the attainable accuracy is influenced by the density and quality of calibration points, the assumptions underlying the calibration model, and the specific requirements of the application. Under typical conditions in the Netherlands, InSAR-based deformation products can be expected to achieve an accuracy on the order of 1 mm yr^{-1} or better.

However, precision and accuracy alone do not fully characterise the quality of PSI-derived deformation estimates. The reliability of the results is strongly influenced by the inherent reliance of PSI workflows on temporal regression modelling. Consequently, the estimated surface deformation should be regarded as a model-derived parameter rather than a direct physical measurement, meaning that the outcome is sensitive to the model formulation and its underlying assumptions. Furthermore, precision is typically inferred from the data itself—either through the scattering properties of the targets or through the residuals obtained after model fitting. To ensure robust and defensible results, it is therefore essential to adopt strategies that mitigate both overfitting and underfitting within the regression framework.

PS-InSAR results are inherently limited to locations that exhibit dominant, temporally stable radar backscatter, which are typically associated with infrastructural elements consistently present across all acquisitions. To enhance spatial coverage, change-detection methods may be employed to identify scatterers that remain coherent only for limited time intervals, often referred to as Robust Scatterers (RS). In addition, many PSI workflows incorporate Distributed Scatterers (DS), which consist of groups of neighbouring pixels ("siblings") from which a common phase component is estimated to improve the signal-to-noise ratio (SNR) in areas lacking PS.

While the inclusion of RS and DS increases spatial coverage, it remains restricted to locations with sufficient temporal coherence, such as dry or homogenous surfaces. In contrast, incoherent areas—most notably vegetated terrain—exhibit highly variable and nonlinear phase behaviour driven by heterogeneous soil and vegetation moisture dynamics, rendering them unsuitable for reliable PSI-based deformation estimates.

3.1.3 Quality control procedures

To ensure the production of high-quality InSAR results, it is essential to establish a clear definition of what constitutes "quality" within the processing chain. This begins with a transparent and well-documented workflow in which both operators and algorithms make structured, traceable, and reproducible decisions. Such transparency ensures that the processing procedure remains controlled, auditable, and repeatable.

Although the absence of a universally standardised PSI workflow allows InSAR service providers to rapidly implement methodological innovations, it also complicates the development of a uniform quality-control framework applicable across all PSI implementations. For this reason, our approach focuses on defining generic quality-control principles that remain valid irrespective of the specific workflow or processing strategy adopted.

Given that the transformation from raw SAR imagery to final InSAR products involves numerous processing stages and intermediate transformations, it is essential to emphasise the need for systematic quality control throughout the entire workflow. Ensuring data integrity at each step helps to prevent the propagation of errors and supports the overall reliability of the final deformation estimates. Within this context, several key quality-control dimensions are identified:

Quality Control Item	Description
Image selection	Images should be evaluated and selected on the basis of the following criteria: - **Coregistration quality:** Each image must exhibit sufficient geometric alignment with the designated reference image. Scenes displaying significant misalignment or limited spatial overlap should be excluded from further processing. - **Perpendicular baseline magnitude***:* The perpendicular baseline relative to the reference acquisition should be assessed, as excessively large baselines (typically > 1 km) degrade interferometric coherence and phase interpretability. Images exceeding this threshold should therefore be discarded.
Atmosphere correction	Following atmospheric correction, the residual noise level as a function of the reference point can be examined to evaluate whether the corrections have been applied effectively. In addition, further quality control steps should be undertaken: - **Inspection for artefacts:** The corrected data should be systematically reviewed to identify potential processing artefacts or anomalous spatial patterns that may indicate insufficient correction or data inconsistencies. - **Exclusion of outlier acquisitions:** Images exhibiting large residuals after correction - suggesting poor atmospheric modelling or degraded coherence - should be removed from subsequent analysis to prevent error propagation.
PS/DS selection	PS and DS measurements must be selected using an appropriate candidate-selection metric, typically derived from the temporal stability of the radar reflectivity. Furthermore, the precision of the estimated deformation parameters can be inferred from the temporal evolution of the phase residuals or other stability indicators. It is essential to evaluate the risk of model overfitting or underfitting during this selection and estimation process, as both can adversely affect the reliability of the resulting deformation time series.
Deformation referencing	The selected deformation reference should be evaluated with respect to the following criteria: - **Suitability for the intended application:** The chosen reference must be appropriate for the specific analytical objective, whether local, regional, or absolute in nature. - **Stationarity**: The reference area or point should exhibit temporal stability, with no significant trends or spatial inconsistencies that could bias the deformation estimates. Where possible, the reference should be validated using independent in-situ measurements, such as GNSS or levelling benchmarks.

	It is important to note that proper referencing is required not only for the estimated linear subsidence rate but also for additional model parameters (e.g., seasonal components or nonlinear trends), which must be anchored to a consistent and rigorously defined datum.
Geolocation referencing	The selected geolocation referencing should be assessed for correctness by visually inspecting the spatial alignment of the PS and DS points on a map and by comparing their positions to established geodetic benchmarks, such as corner reflectors or other precisely surveyed reference targets.

3.1.4 Satellite data used

For this project, we have processed and analysed the InSAR data from two C-band SAR satellites including Sentinel-1 IW and RADARSAT-2 XF during the period from 2015 to 2025. An overview of the satellites' relevant satellite-dependent parameters is found in Table 1.

Table 1. Overview of satellite specifications.

Satellite	Wavelength	Observation period	# of images	Revisit time	Ground range
Sentinel-1	55 mm	2015 – 2025	~440	12 days	5 x 20 m
RadarSAT-2 XF	55 mm	2015 – 2025	~150	24 days	5 x 5 m

A total of five satellite tracks were analysed in the region of interests: two with Sentinel-1 (ascending (asc) track 88 and descending (dsc) track 37) and three with RadarSAT-2 XF (asc tracks 209 and 309 and dsc track 059). The use of multiple satellite tracks over the same area and viewing geometries allows for cross-validation of surface movement patterns and provides increased confidence in the interpretation of the observed InSAR estimates. We have processed and analysed for all stacks the DS as well as PS measurements in LOS. Atmospheric Phase Screen correction (APS) has been applied in all cases to mitigate the phase delays caused by spatially and temporally variable tropospheric conditions; in addition the Sentinel-1 tracks were also processed without APS correction to evaluate the sensitivity of the results due to atmospheric artifacts.

3.2 Geomechanical modelling

A key question in the governance of salt caverns in the Twenthe-Rijn concession concerns their long-term stability. A limited amount of cavern convergence, along with the associated surface subsidence, is acceptable. However, when the roof of a cavern fails and falls down to the bottom, the cavern migrates upward. A propagation of this process towards the surface is a safety issue. The failed material usually occupies a larger volume than it occupied in unfailed condition (this process is called bulking) – but if the distance between cavern roof and surface is not enough, the propagation may reach the surface and cause the abrupt formation of a sinkhole. A way to limit the upward propagation is to inject solid material and reduce the volume that has to be filled by the bulked material. Clearly, however, the early identification of potential cavern failures is important. In the project that we here report we have investigated possibilities to support such evaluations with the use of surface movement measurements and geomechanical modelling. To this end we have first investigated what are the typical signatures or precursors of failure. Then, with the help of observed surface movement estimates using InSAR, we demonstrate how such estimates can be connected to model results and interpreted in the light of potential failure. However, we start with a brief description of the state of the art, using reports made for the operator (Nobian).

3.2.1 State of the Art

Salt mining in the Twenthe-Rijn concession has a long history, dating back to almost a century ago. The operations and associated investigations have resulted in a lot of knowledge and understanding, and a well-developed standing practice for governance. A good entry to that knowledge is formed by the reports by REinvent GmbH, "Update Migration Study" (2023, 2024a-c), created for Nobian, and the parallel publication by Jakob et al. (2025). These reports were not available at the time of start of this project but have proven to provide important information and a valuable source of comparison with our approach.

Cavern leaching in the early days was performed with little control of the resulting cavern geometry. As a result, caverns grew up to the bounding layers above the salt. Later, when it became clear that caverns could migrate upwards after failure of the roof, oil blankets were deployed to ensure a minimum thickness of rocksalt above the cavern. Indeed, because of the salt properties, stresses in the salt tend to be isotropic, making the horizontal stresses larger than in the non-viscous layers above it and providing a barrier against failure of the roof.

However, many caverns existed and still exist in which the leaching has not been optimal. Once roof failure has occurred, an ongoing process of failure can result in migration of the cavern upwards. Solid material from the roof falls to the bottom of the cavern and the void volume migrates. Migration to the surface may result in sinkholes, which form a clear safety issue. Sinkholes must be prevented. This is possible by making use of the bulking behaviour of failed rock: the failed material occupies a larger volume than in its original virgin state. When the volume that needs to be filled is not too large, it may be completely filled before the migration has reached the surface. A reduction of the volume of potentially unstable caverns can be imposed by injecting solid material from outside: filling with, e.g., slurry. This is now practice in the Twenthe-Rijn concession. All existing caverns have been assessed on their risk of failure and associated sinkhole formation, and filling of the caverns takes place after prioritizing their failure risks.

The first report in the "Update Migration Study" series (REinvent GmBH, 2023) and the publication by Jakob et al (2025) identify 5 stages in the development of a cavern, resulting in cavern and subsurface-layer deformation and surface subsidence (Figure 6):

1. Rock salt creep induced
2. Overburden deformation induced
3. Induced by the deflection of the final competent rock layers
4. Induced by the collapse of the final competent rock layers
5. Induced by the consolidation of the bulked overburden

Deformation in Stage 1 was judged to be very small by the REinvent reports, and was not considered further. Stage 2 was considered to occur when some upward cavern migration takes place. Stage 3 will start when a migrating cavern approaches the top of the final competent layer, which is the layer that is overlain by the soft, unconsolidated tertiary or quaternary shallow sediments. The area of influence of Stage 3 is smaller than the area of influence of Stage 2 because the origin is shallower. When the cavern roof above the migrated cavern from Stage 3 fails, the process moves to Stage 4 and a sinkhole will develop with sudden and severe subsidence. However, Stages 3 and 4 do not occur when the cavern migration ends well below the final competent rock layers. Finally, when the cavern is completely filled, consolidation results in further convergence and subsidence. This Stage-5 behaviour follows upon completion of Stages 3 and 4 but can also follow upon the filling of a cavern in Stage 2.

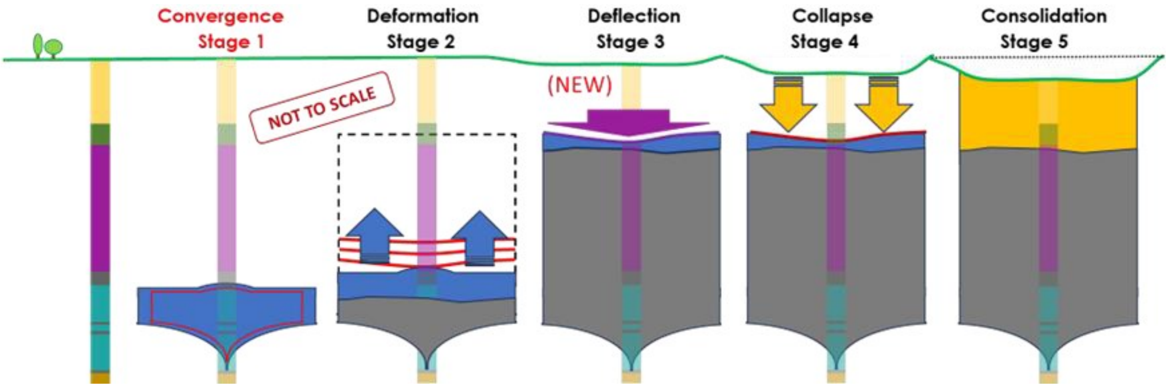

Figure 6. Visualization of the five Stages of cavern deformation, migration and collapse. From Jakob et al (2025).

For the calculation of subsidence originating from salt caverns in the Twenthe-Rijn concession a carefully designed algorithm has been developed (REinvent, 2024a; Jakob et al, 2025). First, the stage of the migration process is determined, along with the associated shape and volume of the cavern and the bending and movement of the cavern roof. Collapse depends on the cavern roof reaching a critical distance to the top of the uppermost competent layer before its volume has decreased to a threshold value. Depending on the stage, a radius of influence at the surface is calculated (R) and the surface profile u_z as a function of the distance from the centre of the subsidence bowl (r) is calculated with an integrated Gaussian function:

$$\boldsymbol{u_z(r)} = \frac{\boldsymbol{S}}{\boldsymbol{2}}\,\mathbf{erf}\left(\frac{\sqrt{\boldsymbol{4\pi}}\cdot\boldsymbol{r'}}{\boldsymbol{R}}\right)\times\left[\mathbf{erf}\left(\frac{\sqrt{\boldsymbol{4\pi}}\cdot(\boldsymbol{r'}+\boldsymbol{r})}{\boldsymbol{R}}\right)+\mathbf{erf}\left(\frac{\sqrt{\boldsymbol{4\pi}}\cdot(\boldsymbol{r'}-\boldsymbol{r})}{\boldsymbol{R}}\right)\right] \qquad \text{Eq. 1}$$

Here, r' is the equivalent radius of the source (the cavern) and S is the subsidence factor representing the underground vertical movement that causes the subsidence. Great care has been taken to ensure smooth transitions between the different stages. The model is called the Bekendam-Jakob-Pinkse (BJP) model.

The expression for the influence function has been derived with a "radius of influence", which depends on the depth of the cavern and the stage of subsidence. The final expression is the result of integrating a Gaussian kernel over a square with sides $2r'$, which breaks the circular symmetry; this choice has presumably originated from the facts that the integral can be analytically given in terms of the well known error function and that the difference with the integral over a circle is marginal.

The algorithm has been applied to the historic development of the Nobian cavern fields within the Twenthe-Rijn mining permit (REinvent, 2024b; Jakob et al, 2025). Ten well-documented historical cavern migration cases dating back from the first two development phases have been assessed with the help of this algorithm. First, the cavern volumes were reconstructed: their original volume; the volume after backfilling (for 7 of them), and their migration upwards. Important information was provided by the monitoring of the caverns. The measured subsidence was assessed in the light of these reconstructed volumes. A validation of the prognosis algorithm was achieved by demonstrating its applicability to 9 of the 10 well-documented cases.

Two more, poorly documented cases were deployed in a reverse operation of the algorithm to reconstruct the migration column and the likely original cavern shape. These cases are interesting in the context of the present investigation. As subsidence data, some levelling data were available, and height maps (Actueel Hoogtebestand Nederland, AHN) in 2012 and 2022. The cases show complex interplay between multiple caverns. The first case, for instance, is a set of 4 interfering caverns where the deepest point in the subsidence bowl is between the two constituting well doublets. As a sidenote, the quantitative data used in the reverse operation consisted of the final value of the subsidence in the centre of the bowl and its location. There was no fit of the temporal development or the areal distribution of the surface movements.

An important question is when to expect cavern migration. REinvent GmbH (2024b) have developed a Cavern Migration Likelihood Scoring System and validated it with the cavern migration cases discussed. This scoring system is based on geomechanics principles in relation to geochemical processes. It combines the possible exposure of the overlying anhydrite layer to water with the cavern geometry and the presence of faults. Interaction between anhydrite and water may result in the formation of gypsum and related deterioration of the rock. Stress concentrations may result, and even tensile stresses can develop. These will pose an additional migration hazard for certain geometries, and when faults are present. The Cavern Migration Likelihood Scoring System that combines these issues resulted in high to very high likelihoods for the well-documented cavern migration cases, thus confirming its applicability.

The Cavern Migration Likelihood Scoring System has been applied to all the caverns in the concession (REinvent GmbH, 2024c). There are no caverns at risk of forming sinkholes at the moment, but the assessment provided a prioritized list of caverns needing backfilling, in order to prevent cavern migration to reach the surface and causing sinkholes in the future.

3.2.2 Numerical Modelling

Caverns in the salt body which originate from salt solution mining can be unstable. As detailed in the previous section, this is related to their geometrical details in the context of the geological situation, the brine pressure inside it, and the possible weakening by geochemical interactions. We have therefore built dedicated models deploying FLAC2D (Fast Lagrangian Analysis of Continua 2D) that mimic typical salt caverns in the Twenthe-Rijn concession area, and evaluated their stability for these attributes.

Well logs of many wells in the area are available on the Netherlands Subsurface Portal (www.nlog.nl). We used the lithostratigraphy of well TWR-015, around which there is considerable subsidence still ongoing. For the cavern dimensions, typical numbers have been chosen from comparing a number of caverns reported by Reinvent (2024b): a cavern with a 100-m radius and a 20-m height. The lithostratigraphy is similar to wells drilled in the neighbourhood. The main layers are indicated in Table 2. Salt creep parameters were chosen according to the creep law formulated by Hunfeld et al, (2022):

$$\dot{\varepsilon}_{axial} = A_1 \exp\left(-\frac{Q_1}{RT}\right)\left(\frac{\Delta\sigma}{\alpha}\right)^{n_1} + A_2 \exp\left(-\frac{Q_2}{RT}\right)\left(\frac{\Delta\sigma}{\alpha}\right)^{n_2} \qquad \text{Eq. 2}$$

Here, $\alpha = 1\,\mathrm{Pa}$ is the reference stress; A_1 and A_2 are the creep strain rate coefficients; Q_1 and Q_2 the activation energies, and n_1 and n_2 the power law exponents. Initial vertical stresses were determined from the weight of the overburden; the horizontal / vertical stress ratio was chosen 0.7 in the elastic layers and 1.0 in the evaporite.

Table 2. Typical lithostratigraphy and mechanical layer properties. For the Evaporite, parameters for a two-branch creep law are additional input.

Layer	Depth Interval (m)	Shear Modulus (GPa)	Bulk Modulus (GPa)	Density (kg/m^3)
North Sea Supergroup	0 – 140	0.40	0.67	2050
Röt Claystone	140 – 330	6.0	10.0	2050
Evaporite	330 – 390	12.7	22.2	2179
Solling Claystone	390 – 500	10.4	13.9	2500
Evaporite	Salt parameters			
	A_1	7e-13 s^{-1}	A_2	2e-34 s^{-1}
	n_1	1	n_2	5
	Q_1/R	3007 K	Q_2/R	6495 K

The modelling strategy was targeted at identifying responses of the overburden that indicate cavern failure. Therefore, after the cavern was constructed and a halmostatic pressure deployed, the brine pressure was reduced in steps of 0.2 MPa. The severe pressure reduction that we deployed is not what happens in reality – we use it here to force failure at a certain point and to investigate effects of different attributes relative to each other. At a certain pressure the roof of the cavern fails in either shear failure or tensile failure mode. Such failure causes loosening of material from the cavern roof which is then falling towards its bottom, gradually reducing the open volume of the cavern by bulking: the failed material occupies a larger volume than it occupied before failure. Migration ceases when the remaining open volume vanishes. In the model, failed zones in the cavern roof were removed from the model in order to attempt to regain a stable model, however, this was usually unsuccessful. This is in line with the report by REinvent (2024b), showing that cavern migration indeed usually stops only by either complete filling by bulked material or by forming a sinkhole. Therefore, the main indications of the simulation were the respective moment and pressure of failure and precursors of it in the shape and speed of the surface movement above the cavern.

The tested geometries are visualized in Figure 7. The base case shows a cavern in the middle of the evaporite layer. Tested variations are a cavern reaching to the top of the evaporite, where a salt roof above it is lacking, and the abstraction of a failed cavern in which the void volume has propagated upwards. Indeed, caverns have been identified that had propagated upward significantly (REinvent, 2024b). For the simulation we consider an open cavern that covers the combined volume of the original cavern and the failed volume, because the bulked material is presumably weak and keeps the balance predominantly by the brine pressure against the boundary of the failed volume.

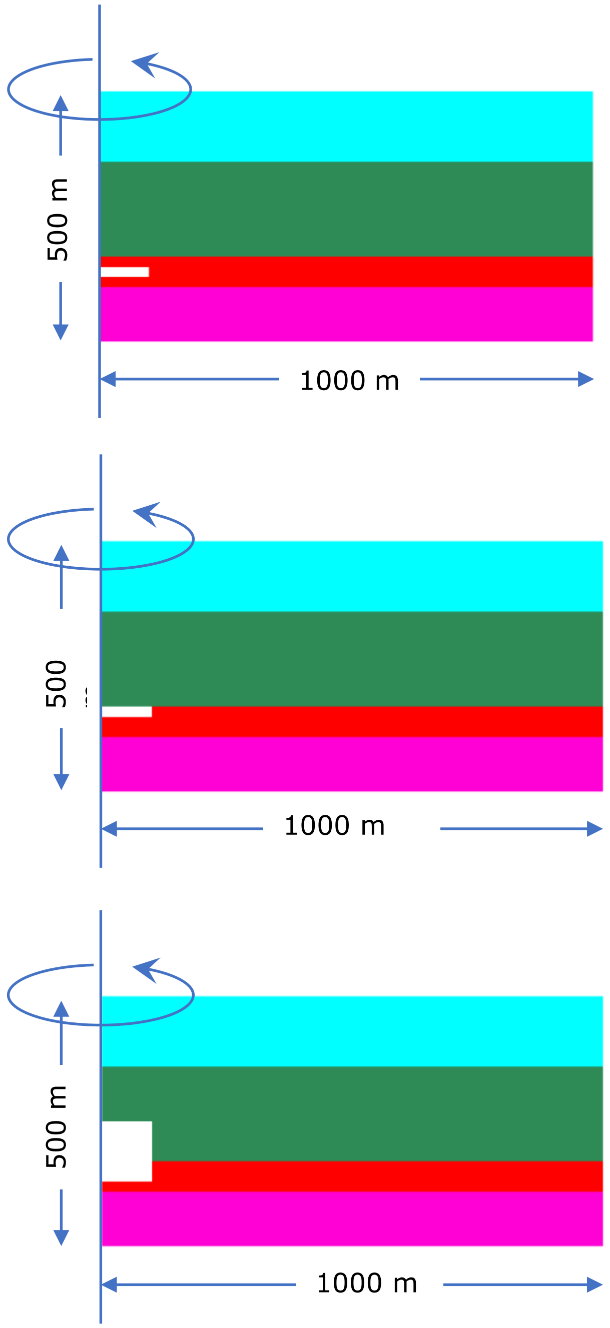

Figure 7. Vertical cross section of three cavern geometry configurations: Cavern in the middle of the evaporite (top); cavern without a salt roof (middle); larger failed volume including cavern and volume above (bottom). The geometry is radially symmetric. Pink and green are clay stone layers, red is the evaporite layer, and blue the North Sea Group layer.

All simulations were performed with a similar schedule. The subsurface model with the cavern was constructed and equilibrated with a high brine pressure: 4 MPa above the halmostatic pressure, close to the lithostatic stress. This resulted in slight surface heave, since this pressure is larger than the lithostatic stress. Then the pressure in the cavern was reduced to halmostatic, and again the brine pressure in the cavern was equilibrated with the mechanical response around it. This situation mimics the initial leached cavern. The elastic response of the subsurface gives an immediate surface subsidence. The pressure then was reduced in 0.2 MPa steps, with periods of 3 months between the pressure reduction steps, in which salt creep was allowed to act. The simulation was stopped when no equilibrium could be achieved anymore.

The modelling strategy is not completely in line with the actual mechanical processes around the caverns. We have neither modelled pore pressures in the layers overlying the evaporites, nor have we incorporated layer separation and possible pressurization of space thus created that might precede roof collapse. We have focused on the temporal and spatial signatures that originate from failure and that precede it. This renders our simulations mainly indicative, but it does enable a comparative study of the effect of different attributes.

The simulation of the base case shows a stable cavern up to highly reduced brine pressures. Starting from a halmostatic pressure (with a brine density of 1200 kg/m^3) we see that the salt roof effectively stabilized the subsurface. This is related to the creep behaviour of the salt, which tends to equalize the principal stresses. Failure occurs only when the stresses become tensile or when the shear stresses above the cavern exceed the Mohr-Coulomb failure criterion for a limited time after a pressure change and before creep has equalized the pressure. Shear failure in the layer above the evaporite can only cause cavern failure if the cavern actually has a boundary in that layer – which is the case for the cavern without salt roof.

As an example output we visualize the stresses and vertical displacements of the base case after 11 months, 2 months after the pressure has been reduced to 0.6 MPa below halmostatic (Figure 8 and Figure 9). Stresses around the cavern have been mostly equilibrated to stable values, except for a small area near its edges – this may be a numerical artefact. Far away from the cavern, the shear stresses are near zero in the salt, while non-zero stresses remain present in the other layers. Further, we see that convergence of the cavern has mainly taken place by moving upwards of the bottom and downwards of the roof.

The base case fails after 51 months and a pressure decrease of 3.4 MPa. The failure results in an increase of the cavern volume by part of the roof falling down, however our FLAC2D simulation failed to reach equilibrium (Figure 10).

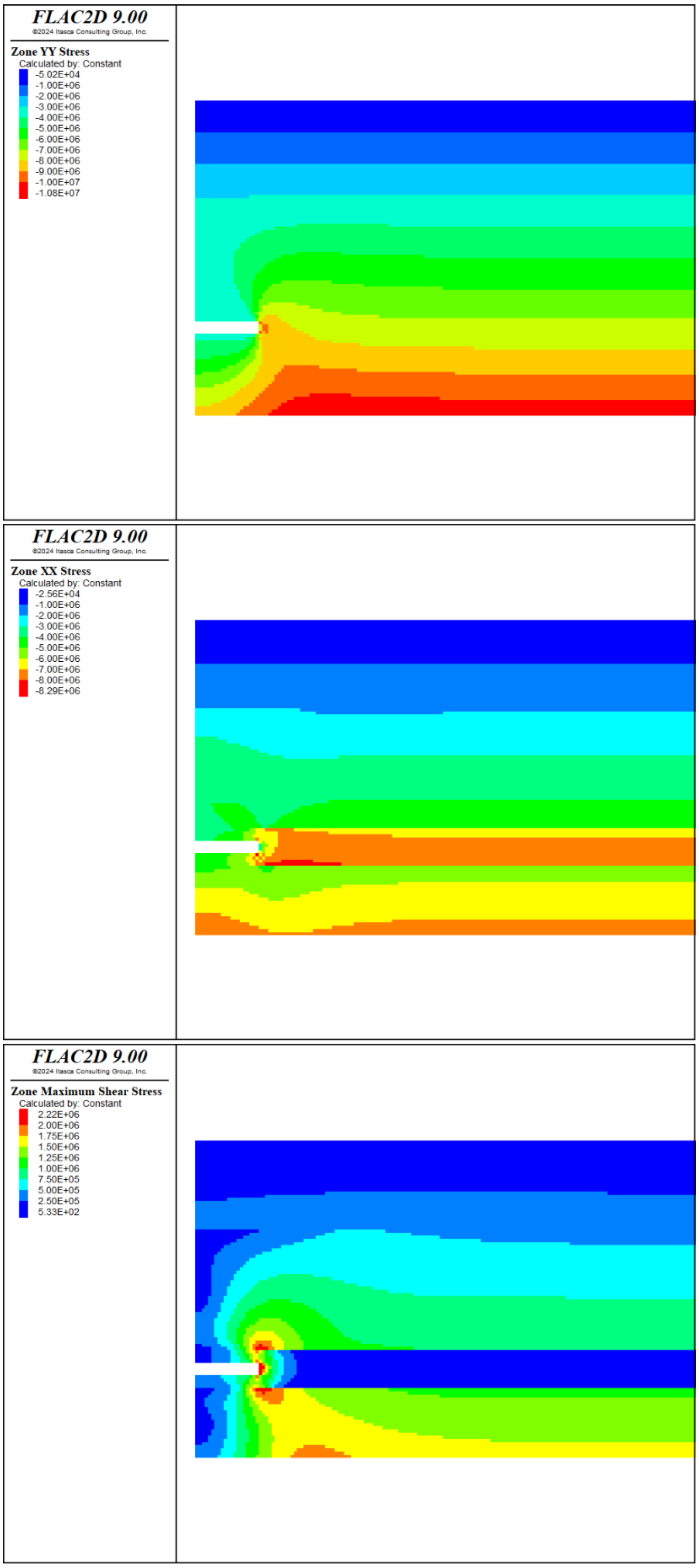

Figure 8. Vertical (top), radial (middle), and maximum shear (bottom) stresses after 11 months of simulation of the base case, with the brine pressure 0.6 MPa below halmostatic.

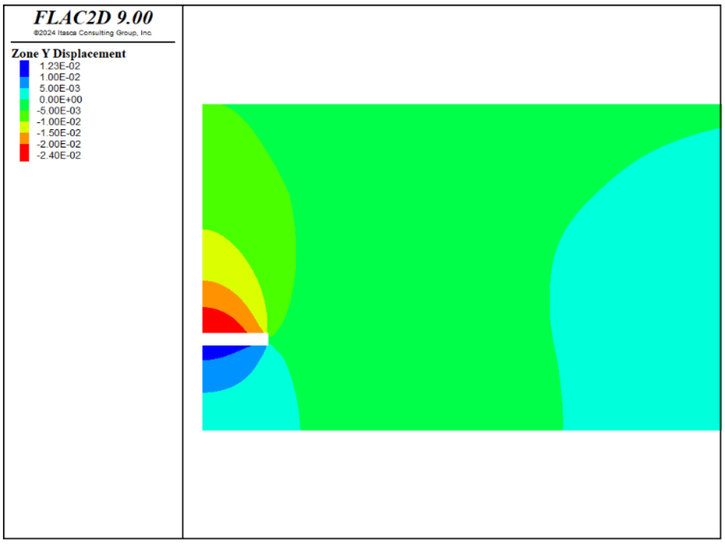

Figure 9. Vertical displacements 11 months of simulation of the Base Case, with the brine pressure 0.6 MPa below halmostatic.

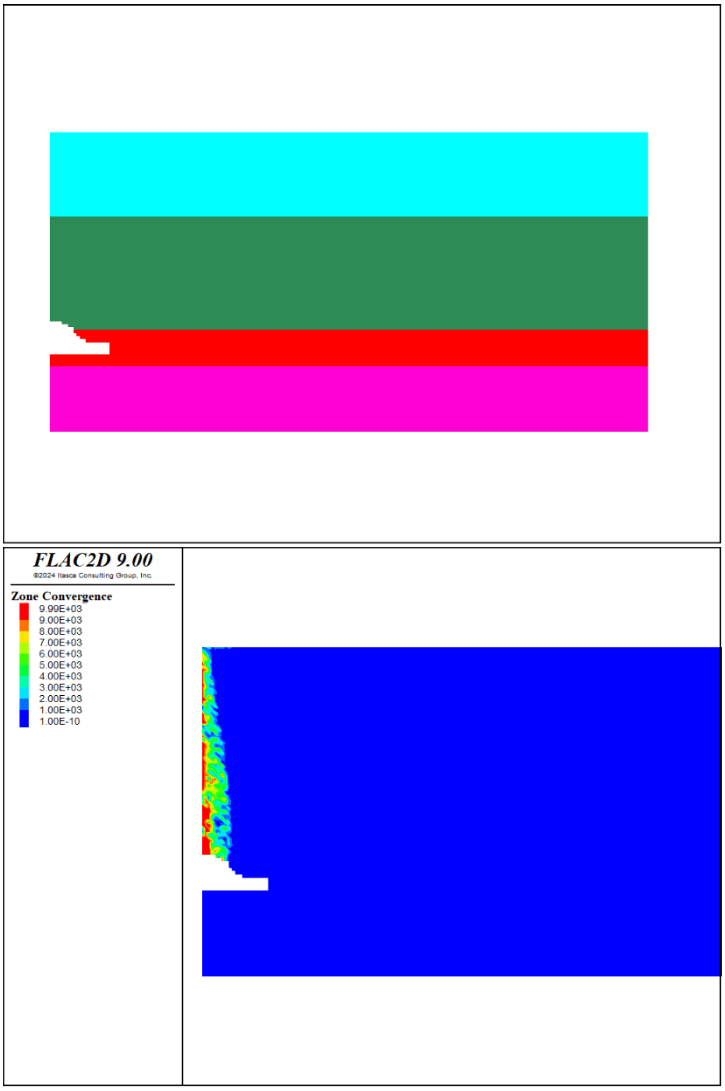

Figure 10. Results of final simulation step of the Base Case. Top: geometry with cavern. Bottom: Convergence (measure of simulation result quality)/ No numerical stability was achieved.

Including the base case we have formulated 7 scenarios. They are summarized in Table 3.

Table 3. Definition of sensitivities for modelled scenarios. The cases other than the Base Case (Elastic, Fast creep, etc.) are formulated with respect to the Base Case, of which the parameters are provided in Table 1. K0 is the horizontal/vertical stress ratio.

Base Case	**Elastic**	**Fast creep**	**Large Cavern**	**No roof**	**No roof, low K_0**	**No roof, high K_0**
Input: Tables 1 & 2	No creep in Evaporite	10 times faster creep in evaporite	Top cavern 100 m shallower	Top cavern against top salt	Top cavern against top salt; K_0 = 0.6	Top cavern against top salt; K_0 = 0.8

A major outcome of the calculations is the surface movement. Since the model is not representative for the actual situation and the subsurface and salt parameters are subject to considerable uncertainty we provide a mainly comparative discussion of the results. We compare the results of a number of scenarios after reaching a comparable amount of subsidence above the centre of the cavern. Curves for the radial and vertical surface movement of the first 5 cases are given in Figure 11. Most scenarios give very similar surface movement distributions. Only the case with the larger cavern, reaching far into the elastic clay layer above the Evaporite, results in a narrower profile. In the next section we will use the two qualitative signatures in a comparison with the movement that was actually observed in the surface subsidence by InSAR in the area around cavern TWR-014.

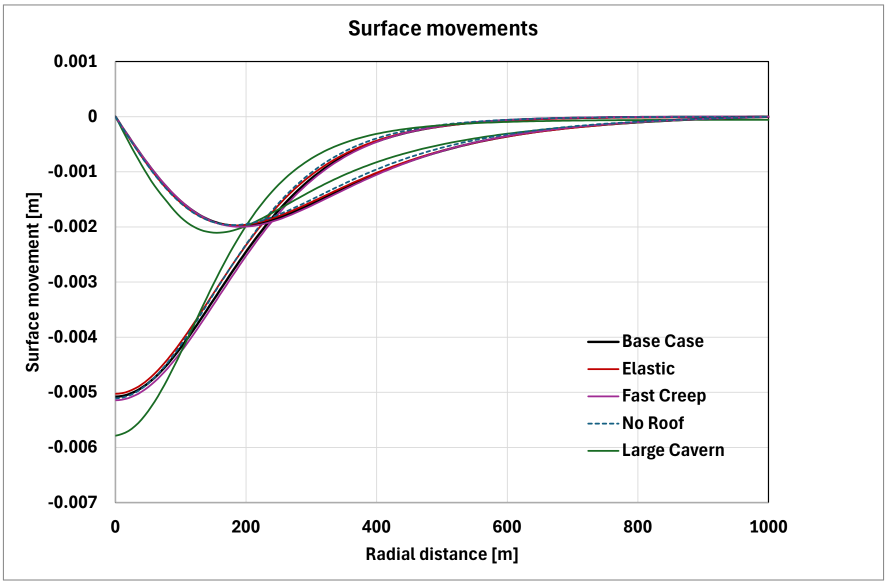

Figure 11. Radial and vertical surface movement for 5 scenarios. Only the large cavern results in a different shape of the surface movement signature. Radial displacement curves are starting at zero displacement in the centre (radial distance = 0). Y-axis is the surface movement (m) and x-axis the radial distance (m) from cavern centre.

Figure 12 shows the temporal development of the vertical movement above the cavern upon reducing stepwise the brine pressure in the cavern for the 7 scenarios defined above. As discussed, the Base Case results in a long-lasting stable subsidence. For the last timesteps, the immediate response after pressure reduction becomes larger. A very similar profile is observed for the Elastic Case. The main difference with the Base Case is the absence of creep during the repeated periods of three months between the pressure reduction steps. Conversely, the case with the increased creep rate coefficients results in a larger subsidence velocity than the Base Case. The moment of failure here also comes at less reduction of the pressure, presumably because of larger deformations at the cavern roof.

The geometry of the starting cavern has a pronounced effect. Figure 12 demonstrates how the cavern stability is compromised much earlier when the salt roof is absent. The three cases without a roof show failure at pressure reductions between 1.2 and 1.8 MPa. Both the increase and the decrease of the horizontal stress ratio (K_0) causes a lower critical pressure reduction than the standard value. The cases highlighted in Figure 12 demonstrate some of the key situations present in the Twenthe-Rijn concession.

An even bigger effect was observed with the simulation with the large cavern. This scenario was constructed to mimic an already failed cavern with loose material inside. When the material has bulked considerably there may still be scope for easy compression and our approach of using a large body of material which behaves as a fluid might be a good modelling option. Besides the effect noted with respect to the shape of the subsidence pattern, there is a much earlier failure. However, since the after-failure simulations are not stable and the pressure boundary condition is not physically representative for the failed and filled cavern, we draw no further quantitative conclusions from the earlier massive failure in this simulation. We will just use the resulting different shapes.

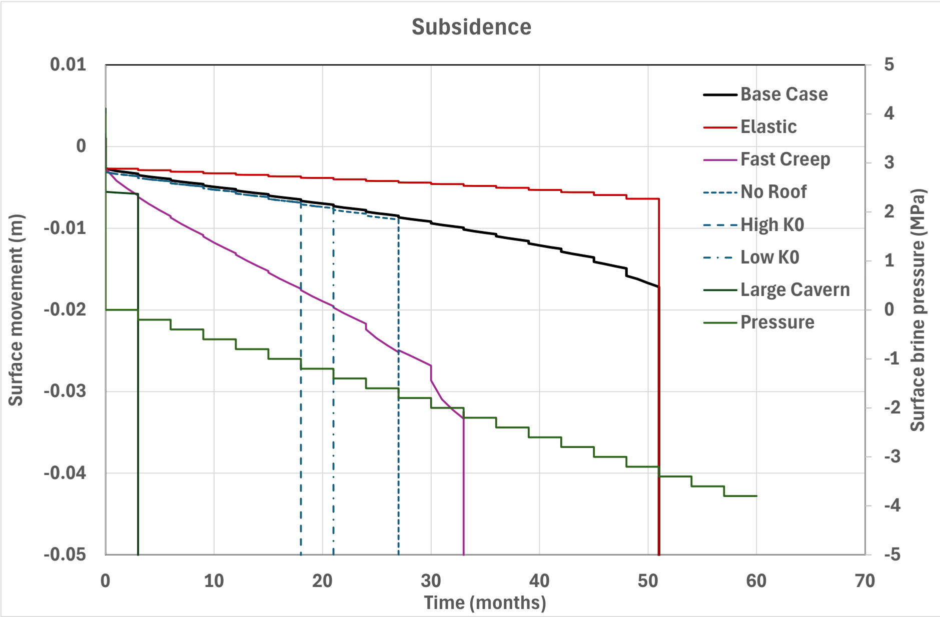

Figure 12. Development of the subsidence above the cavern for the seven scenarios defined in Table 2. Left y-axis is the surface movement (m) and the right y-axis the surface brine pressure (MPa); x-axis gives the time in month.

Improvements of the simulation strategy can be achieved at a number of points. The main improvement will be to have a better representation of the subsurface processes. Incorporation of pore pressures and effective stresses will bring absolute numbers of the onset of failure closer to reality. Another improvement is the incorporation of weakening that will happen due to mechanical and geochemical interactions, or that may be inherent to the material studied. Weakening will induce regions of increased strain rates, so-called shear bands. This may lead to adjustments of the surface movement profiles. Further refinement may come from the geometrical representation of the caverns. The current modelling assumes cylindrical shapes; this could be tuned towards more representative geometries with rounded edges to decrease numerical instabilities. Grid refinements might help here as well. Finally, a big step would be when the actual post-failure behaviour could be modelled. The newest release of FLAC2D facilitates multiple point modelling and remeshing, which enables following the failed material in a completely new manner. Then, modelling the actual development of sinkholes come within the scope of the tools engaged.

The value of the current simulations is in connecting its insights to the monitoring of land movement by means of InSAR. The first attribute, therefore, is the temporal development of the land movement. A collapse of a cavern, and the expected upwards migration after it, is usually preceded by an acceleration of the subsidence rate. Of course, changes in surface movement rates were also clear from the modelling of the 5 stages of cavern convergence identified by REinvent (2023), but the current results also show precursors, signs of acceleration before collapse. More targeted modelling could better quantify that.

A second issue is the shape of the subsidence bowl. Caverns which have migrated to the surface cause deeper and narrower subsidence bowls. The extreme case, of course, is a sinkhole, which has lateral dimensions of the order of the cavern diameter. Here, the most important attribute of the modelling becomes apparent: the derivation of displacements in every direction. This is of particular value because it can be connected to the current-day InSAR estimates of the surface movement in the different Line-Of-Sight direction of ascending and descending satellite modes. In the next Section we will show how the InSAR-derived movements in the Line-Of-Sight direction can be connected to modelling results.

4. Results and Discussion

4.1 InSAR results and observations

To analyse and interpret the InSAR data we have taken into account the following criteria:

- Linear velocity (mm/yr) (hotspots)
- Spatial patterns
- Accelerations/decelerations (mm yr^{-1})
- Correlation with boreholes

We identify two regions of interest based on the aforementioned criteria: 1) the region just south of the Nobian factory at the *Boortorenweg* and 2) an area north-east of Beckum, around the *Beckumerstraat* (Figure 13).

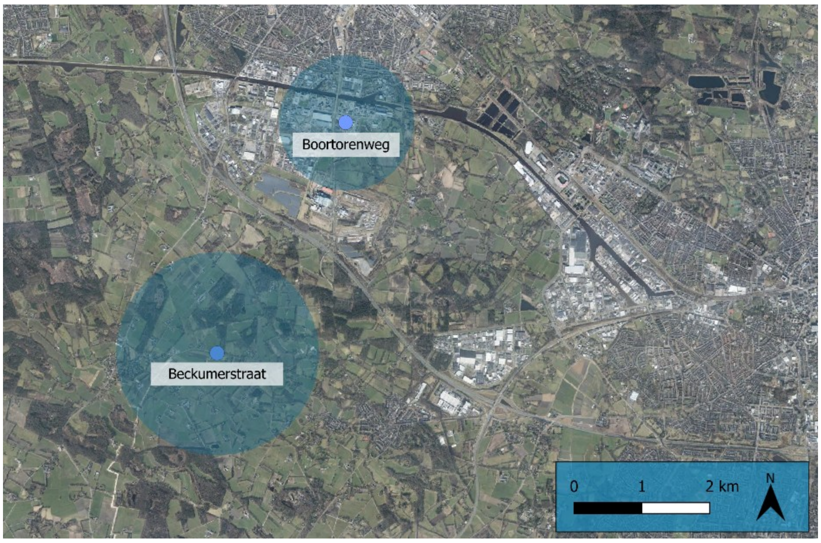

Figure 13. Overview of locations of interest with regards to surface deformation in the Twente salt-mining region.

- The *Boortorenweg* location shows a pronounced and spatially coherent deformation signal in the LOS measurements across all satellite tracks. At this location one of the underground caverns had collapsed in the past and the signal picked up is most likely the aftermath. Therefore, the spatial concentration and temporal coherence of this signal are consistent with expected subsidence processes. This location also correlates well to borehole locations in the area. Linear deformation observed is in the order of -5 to -15 mm/yr.

- The *Beckumerstraat* location shows a small linear deformation (> -2 mm/yr), but spatially correlated signal. As the location corresponds to available borehole locations, it is considered a relevant signal for this study.

- The *Zouthuisje* (salt extraction facility) is a third location due to a highly localized subsidence signal identified in one of the ascending Sentinel-1 interferometric stacks. This deformation anomaly spatially coincides with a known borehole. This example illustrates that InSAR is capable of detecting very localized surface deformation patterns; however, it also highlights that satellite acquisition parameters—such as imaging geometry, incidence angle, and time of acquisition—as well as local constructions/renovations can influence the detectability and consistency of deformation signals across tracks and satellites. Because the observed subsidence pattern was not consistently present across the different Sentinel-1 stacks, nor RadarSAT-2 stacks, no further analysis of this location was pursued. An example of such local deformation signal is shown in Appendix C InSAR results at *Zouthuisje*.

4.1.1 Boortorenweg

At the *Boortorenweg* the deformation signals are consistent across all the sensor tracks. For the detailed analysis, we considered only PS datapoints with APS correction as these provide the most spatially coherent deformation estimates. This area is known to have experienced severe cavern migration, and the observed deformation signal is most likely a continuation of its post-collapse subsidence. Figure 14 presents the LOS deformation results for one RadarSAT-2 track (T209), including both PS and DS estimates. This location has been identified as a hotspot, as linear deformation rates exceed -5 mm/yr, show a clear spatial correlation with borehole locations, and exhibit a deformation pattern consistent with the expected radius of influence of the underlying salt cavern. The hotspot is detected by both satellite datasets and is particularly distinct in the PS results, owing to the abundance of infrastructure in the area.

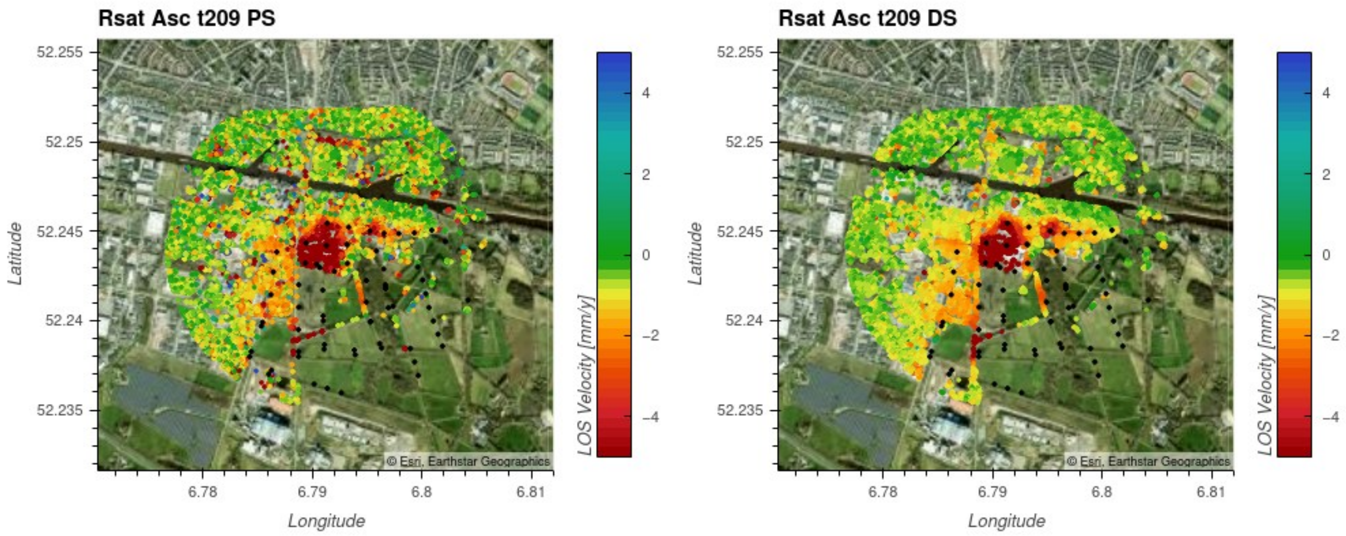

Figure 14. LOS InSAR PS (left) and DS (right) results of RadarSAT-2 XF ascending track T209 at the Boortorenweg. Atmosphere correction has been applied. Black dots are borehole locations.

Due to the dynamics of a salt cavern, the surface is expected to move horizontally toward the point directly above the centre of the cavern. This means the total ground-movement direction lies in a vertical plane defined by the observation point and the vertical line above the cavern.

To show this clearly, we selected a horizontal line (from A to B in Figure 15) that passes through the expected centre of the subsidence bowl and aligns with the satellite LOS direction. Along this line, the ground movement projected onto the LOS direction can be treated as a two-dimensional slice.

We averaged the LOS velocities in 20-meter distance intervals from the centre along this line (Figure 16). The results show that the maximum movement—and the entire movement profile—appears slightly farther west for the ascending satellite tracks compared to the descending tracks. This difference is caused by the horizontal movement component affecting the LOS projection. In the ascending stacks a number of outliers are observed which can be related to noise in the observed signal, potentially cause by on the ground construction in the east of the subsidence centre, only picked up by the ascending track. A more strict filtering on quality can be applied to get rid of these noise effects at the cost of point density. For this demonstration it was not deemed necessary.

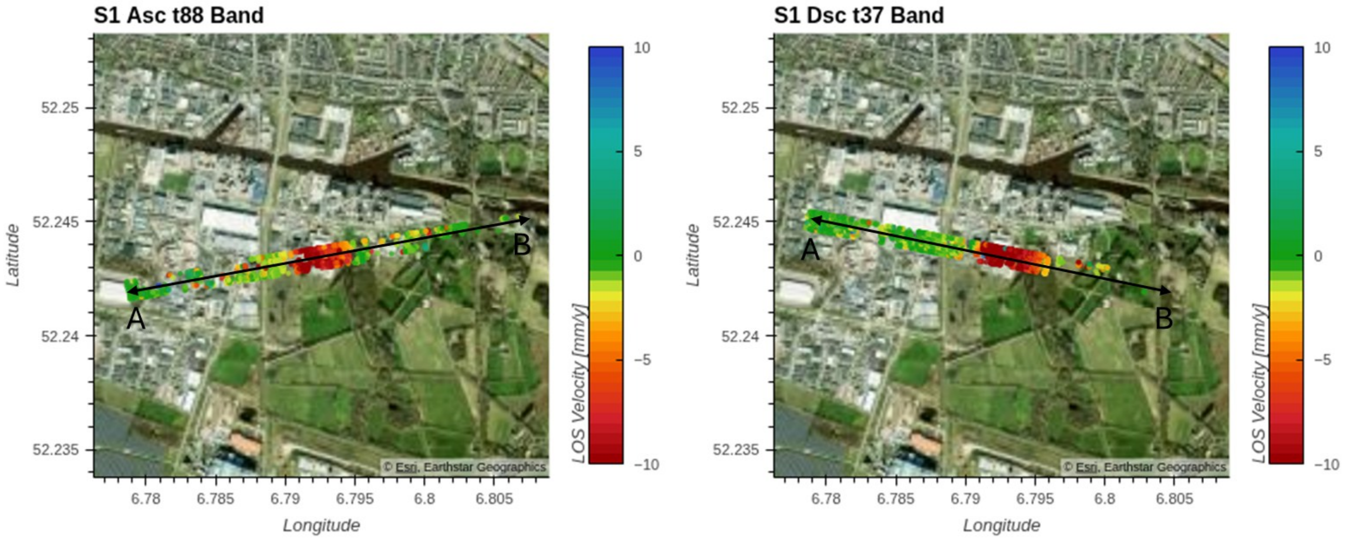

Figure 15. Sentinel-1 InSAR LOS results in band perpendicular to satellite flying direction at the Boortorenweg. Longitude and Latitude in EPSG 4326. Left: satellite looking from west to east. Right: satellite looking from east to west. Cross-section A-B corresponds to the average velocity graph in Figure 16.

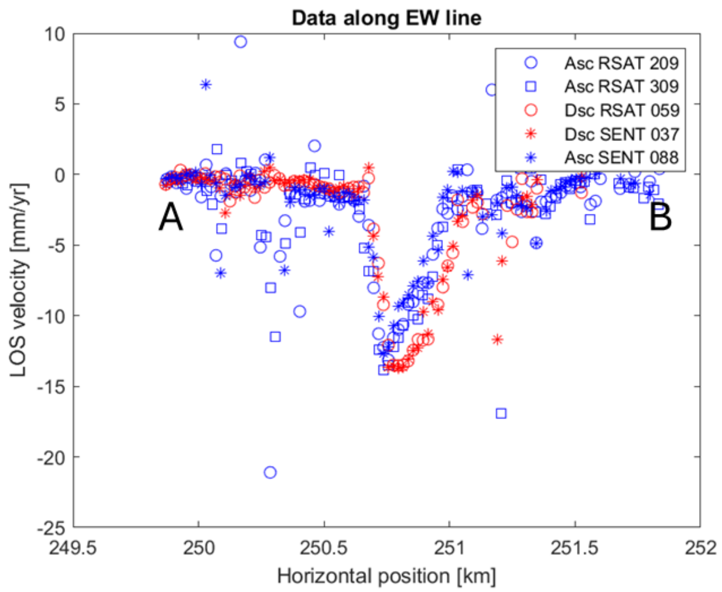

Figure 16. Averaged velocity in the LOS direction in 20-m intervals, in the EW bands perpendicular to the direction of satellite flight (A-B in Figure 15).

InSAR LOS results of all stacks for the *Boortorenweg* are visualised in Appendix A InSAR results at *Boortorenweg*.

Next to linear deformation, we also observed a slight deceleration (around 0.4 – 0.5 mm/yr/yr) of the surface deformation at this location (see Figure 26 in Appendix A InSAR results at *Boortorenweg*). As this location experienced a collapse in the past, the deceleration of the deformation is expected, as the ground moves into equilibrium again. This deceleration pattern has not been noted at other locations in the region.

4.1.2 Beckumerstraat

At the *Beckumerstraat* a distinct spatial pattern of ground deformation is evident in the InSAR data. This pattern is consistently observed across all satellite tracks, yet it is most pronounced in the RadarSAT-2 XF data, likely due to the sensor's higher spatial resolution. Figure 17 shows the PS and DS estimated for one asc RadarSAT-2 track, while Figure 18 presents the results of the asc Sentinel-1 track over the same area. The deformation magnitude at this site is approximately two times smaller than that observed at the *Boortorenweg* location, and therefore this site is considered a comparatively less significant deformation hotspot.

A comparison of the different satellite results highlights the added value of DS processing in rural area. Owing to the finer spatial resolution of RADARSAT-2 XF, the point density—and consequently the spatial coverage—is substantially higher than for Sentinel-1. Although a weak spatial deformation pattern remains detectable in the Sentinel-1 PS results, it becomes clearly discernible only when isolating this area from the broader study region.

The LOS InSAR results for all tracks per satellite over the *Beckumerstraat* are presented in Appendix B InSAR results around Beckumerstraat. All RadarSAT-2 tracks exhibit a consistent deformation pattern in this area, although the descending track shows slightly lower subsidence rates than the ascending tracks. This discrepancy may be related to a higher proportion of coherent observations originating from buildings with strong foundations, rather than from the ground surface itself. Differences between the ascending and descending results might also be caused by the presence of horizontal deformation. This causes an offset in location of the subsidence pattern between the ascending and descending results, as can be observed on the *Boortorenweg* location.

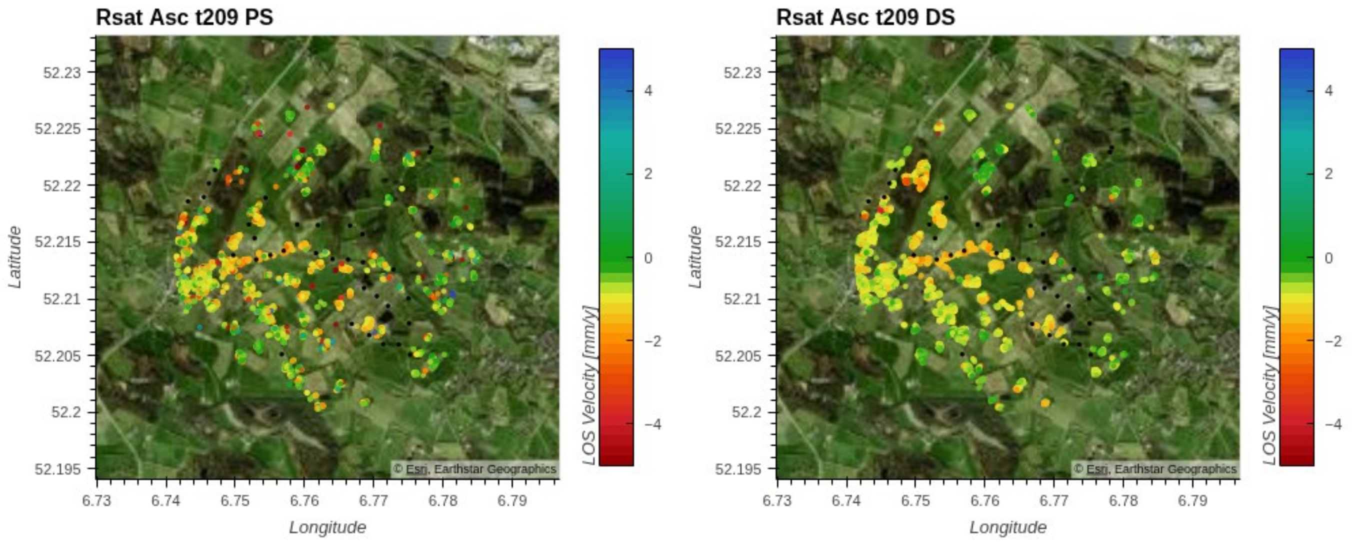

Figure 17. RadarSAT-2 InSAR results for ascending track 209, PS and DS at Beckumerstraat. Correction has been applied for the atmosphere (with APS). Black dots are borehole locations.

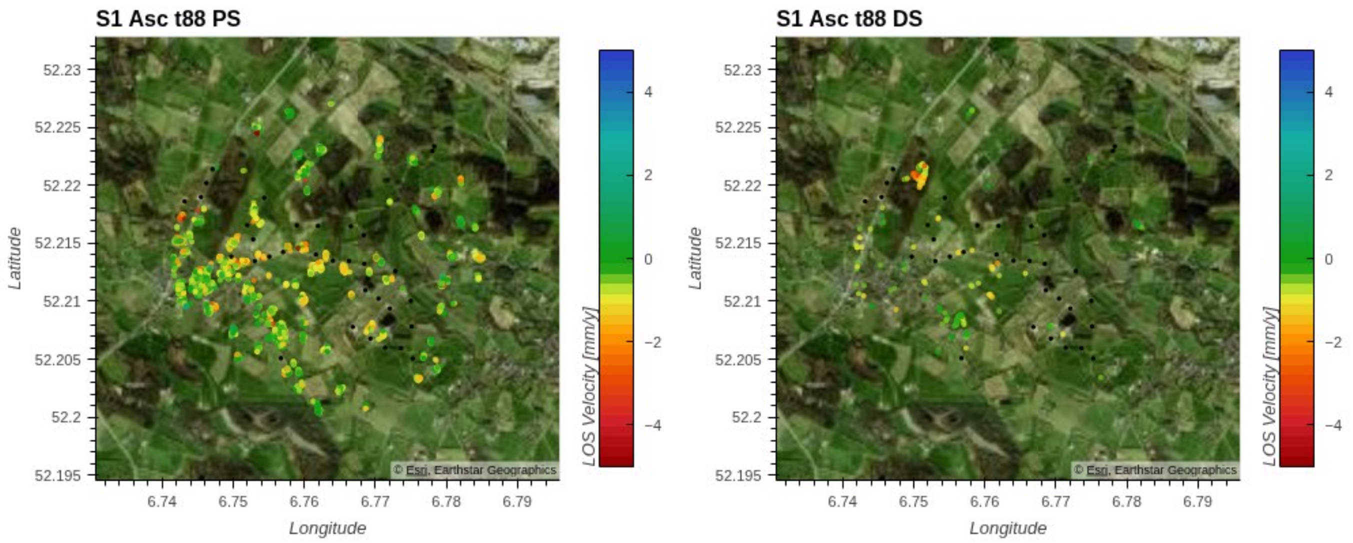

Figure 18. Sentinel-1 InSAR results for ascending track 88, PS and DS at Beckumerstraat. Correction of atmosphere has been applied (with APS). Black dots are borehole locations.

Interpretation of the data at these locations leads to some general observations that are deemed relevant for the application of InSAR for monitoring mining areas.

Point density and coverage:
For both study areas mentioned above, the higher spatial (ground-range) resolution provided by RadarSAT-2 results in substantially improved spatial coverage. Smaller road segments - such as at the *Beckumerstraat* - exhibit a higher density of coherent scatterers in RadarSAT-2 stacks compared to Sentinel-1 (see Figure 27 and Figure 28 in Appendix B). This effect is particularly pronounced in rural environments, where extensive vegetation and limited paved infrastructure reduce the availability of stable reflectors. In such contexts, increased radar resolution is critical, as it enhances the ability to detect and delineate spatially correlated deformation patterns. This is especially relevant for assessing mining-induced subsidence. The benefits of higher resolution are most evident in the area surrounding Beckum, where paved surfaces are sparsely distributed and consequently the number of coherent measurement points is limited.

Besides spatial resolution, the type of scatterers used also influences the coverage in rural areas and hence the detection of spatially correlated deformation patterns. For RadarSAT-2 the number of DS obtained in the Twenthe-Rijn region is significantly larger than for Sentinel-1, which can be related to the difference in spatial resolution (see Figure 24 and Figure 25 in Appendix A InSAR results at *Boortorenweg*). When changes on the ground take place (e.g. constructions), PS measurements are lost over time. By applying change detection to generate RS, we are able to receive scatterers that remain coherent only for limited time intervals, leading to improved spatial coverage and detection of coherent sub-periods. To observe spatial patterns over the area, the processing of DS and RS is therefore highly recommended and PSI settings need to be optimized for the location of interest.

Temporal resolution:
Sentinel-1 provides an acquisition approximately once per week, whereas RadarSAT-2 has a repeat interval of 24 days. For the present application, no clear advantage is observed from the higher temporal sampling of Sentinel-1 relative to RadarSAT-2. This is likely attributable to the expected temporal characteristics of the deformation phenomenon: mining-induced subsidence in the study area is not anticipated to evolve rapidly on weekly timescales. Consequently, the additional temporal density offered by Sentinel-1 does not translate into a measurable improvement in the deformation time series. However, higher temporal resolution may become increasingly important when approaching the onset of structural instability or collapse, when non-linear deformation behaviour and accelerated ground movement are more likely to occur (see model scenarios in Figure 12).

Atmosphere correction:
Atmosphere correction is typically included as standard component of the quality-control workflow in PSI processing (see Section 3.1.3).
In most cases, atmospheric phase delays are mitigated by exploiting their characteristic behaviour: they are spatially correlated yet temporally uncorrelated, allowing separation from deformation signals that evolve coherently over time. At the outset of this study, it was hypothesised that mining-induced subsidence in the area of interest might also exhibit spatially correlated deformation patterns. If this were the case, applying the standard atmospheric correction procedure could inadvertently remove or attenuate components of the true deformation signal present in the InSAR observations.
To evaluate this risk, PSI processing without atmospheric correction was performed on the Sentinel-1 stacks. The results, however, show no significant differences compared with the atmospherically corrected datasets (Figure 23 and Figure 24 in Appendix A). This outcome can be attributed to the limited presence of non-linear temporal deformation in the study region and the relatively small size of the area processed. The two locations where spatially coherent deformation is observed display predominantly stable or linear temporal behaviour, meaning that atmospheric filtering does not interfere with the retrieval of the deformation signal.

4.2 Model inversion results

The FLAC2D models provide surface displacements in the vertical and horizontal (radial) directions. After a coordinate transfer to cartesian (x-y-z) coordinates, these can be projected upon the LOS direction of the different InSAR missions and tracks, so a direct comparison between model and InSAR-estimated movements can be made.

For the phenomenological correlations used by REinvent GmBH (2024a) and Jakob et al (2025), only vertical displacements are provided (Eq. 1). However, with some assumptions we can estimate the horizontal movements associated with the vertical movements for this model. Sroka et al (2017) state that the horizontal displacement is commonly proportional to the derivative of the vertical displacement. They use a Gaussian subsidence profile:

$$
\begin{aligned}
u_z(r) &= u_{max} \cdot \exp\left(-\pi \frac{r^2}{R_{Sroka}^2}\right) \\
u_r(r) &= -\lambda R_{Sroka} \cdot \frac{du_z}{dr} = -\frac{2\pi r \lambda}{R_{Sroka}} \cdot u_{max} \cdot \exp\left(-\pi \frac{r^2}{R_{Sroka}^2}\right)
\end{aligned}
\quad \text{Eq. 3}
$$

With this model, a proportionality factor close to $\lambda = 1$ for salt caverns in the Etzel cavern field in Germany was found. A lower value of $\lambda = 0.4$ was reported for hard coal mining, and also used in calculations for the Epe mines.

Because REinvent use an influence radius that is twice the influence radius of Sroka et al (2017), the derivative of Eq. 1 must be multiplied by $0.5 \cdot R$ to obtain the horizontal movement. We obtain:

$$
\begin{aligned}
u_z(r) &= \frac{S}{2} \operatorname{erf}\left(\frac{\sqrt{4\pi} \cdot r'}{R}\right) \times \left[\operatorname{erf}\left(\frac{\sqrt{4\pi} \cdot (r' + r)}{R}\right) + \operatorname{erf}\left(\frac{\sqrt{4\pi} \cdot (r' - r)}{R}\right)\right] \\
u_r(r) &= \lambda S \operatorname{erf}\left(\frac{\sqrt{4\pi} \cdot r'}{R}\right) \times \left[\exp\left(-\frac{4\pi \cdot (r' + r)^2}{R^2}\right) - \exp\left(-\frac{4\pi \cdot (r' - r)^2}{R^2}\right)\right]
\end{aligned}
\quad \text{Eq. 4}
$$

From geomechanical considerations, a Gaussian profile is not expected. Fokker and Osinga (2018) provide expressions for the influence functions originating from a centre of compression and from a vertical double force. These expressions can represent a contracting or expanding sphere and a contracting or expanding horizontal circular crack, respectively. The centre of compression source is equivalent to the well-known Geertsma or Mogi sources (Geertsma, 1973); (Mogi, 1958). Fokker and Osinga (2018) also show that these influence functions concur with numerically derived influence functions from localized contracting or expanding sources of such shapes. We therefore formulate integrals of these functions here in the same spirit as the BJP influence function (Eq. 4). The subsidence profiles for a point source are:

$$
\begin{aligned}
u_{z,Geertsma}(r) &= \frac{1-\nu}{\pi} \cdot \frac{D}{R^3} \\
u_{r,Geertsma}(r) &= \frac{1-\nu}{\pi} \cdot \frac{r}{R^3} \\
u_{z,DF}(r) &= \frac{1-\nu}{\pi(2-4\nu)} \cdot D \cdot \left\{\frac{2\nu}{R^3} - \frac{3D^2}{R^5}\right\} \\
u_{r,DF}(r) &= \frac{1-\nu}{\pi(2-4\nu)} \cdot r \cdot \left\{\frac{2\nu}{R^3} - \frac{3D^2}{R^5}\right\} \\
R &= \sqrt{r^2 + D^2}
\end{aligned}
\quad \text{Eq. 5}
$$

The integrals of these functions over a square of dimension $2\boldsymbol{R_{cav}}$ are given in Appendix E.

We ran a number of simple inversion exercises to match the interpreted LOS InSAR data to the models available. For the FLAC models, we used the profiles of the Base Case and of the Large Cavern model, as the shapes of the others were very close to the Base Case results. There were three model parameters to be matched: the position of the cavern in x and y, and the strength of the subsidence source.

We also performed inversions with analytical influence functions. Those are detailed in Appendix E. For the BJP model (Eq. 4) there were 5 or 6 parameters to be matched:

- the position of the cavern in x and y,
- the strength of the subsidence source,
- the radius of the influence, the radius of the cavern and
- optionally the parameter λ.

For the Geertsma and Double Force models we had 5 parameters: the position of the cavern in x and y, the strength of the subsidence source, the depth of the source and the radius of the cavern. The matching was performed with the data of the 5 tracks simultaneously. The quality of the match is expressed in χ^2, which is the cumulative squared mismatch between model estimate and InSAR-derived estimate of the surface movements. A lower value of χ^2indicated a better match. Numerical results of the inversions are provided in Table 4.

Table 4. Inversion results with the different subsidence models. Italic number in the table (*) were given, not optimized.

Case	X_{RD}^{cav} **(km)**	Y_{RD}^{cav} **(km)**	**Strength (a.u.)**	R_{Infl} **or** D **(m)**	R_{Cavern} **(m)**	λ **(-)**	χ^2 **(10^6 m²/y²)**
BJP ($\lambda = 1$)	250.84	473.70	10.5	183	164	*1 (*)*	1.037
BJP ($\lambda = 0.4$)	250.83	473.69	14.4	344	150	*0.4 (*)*	0.973
BJP	250.83	473.68	61.3	596	78	0.15	0.954
FLAC BC	250.84	473.67	1973	*350 (*)*	*100 (*)*		0.999
FLAC LC	250.83	473.69	349	*250 (*)*	*100 (*)*		0.962
Geertsma	250.83	473.69	516	163	113		0.958
Double Force	250.83	473.68	734	268	98		0.948

The data for the Sentinel tracks and the results for the LOS calculations with the optimized model parameters are represented in Appendix D Model results at *Boortorenweg*. The quality of the model match can also be recognized in the plots with the residuals. The BJP match with free λ and the FLAC match with the large cavern catch some of the detail at the edge of the cavern. However, for the match with the BJP function, the value of λ of 0.15 is very small, and outside the bounds reported in the literature. The quality of the match with the influence function from the large-cavern FLAC model is remarkably good – especially in view of the fewer matched parameters. The match with the analytical influence functions from the Geertsma and Double Force sources is also good – the Double Force gives the best results of all (Figure 19).

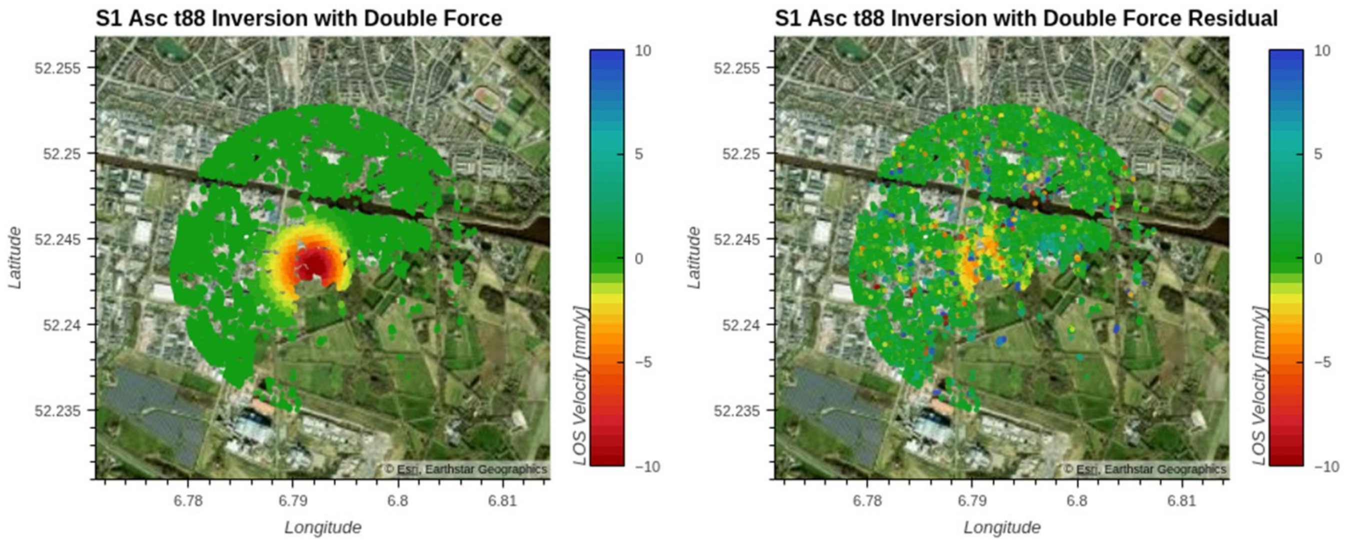

Figure 19. Model inversion (left) and residuals (right) for the LOS measurements of the ascending Sentinel-1 track 88 using the Double Force model. Colours show the velocity (mm/y) of the surface, which red indicating subsidence and blue uplift.

As a graphical representation for clarification, we have also calculated the displacements on the LOS position as shown in Figure 16. We see that the profiles of the descending tracks have their largest value more towards the west, and that this is indeed reproduced by the models (Figure 20 and Figure 21). This is related to the contribution of the horizontal movements to the movement along the LOS. Further, we see that the FLAC model with the large cavern is representing the InSAR data better than the BJP models and the base case FLAC model. Outliers to the east of the subsidence centre are most likely cause of noisy measurements, which have an effect on the calculated residuals. A more strict filtering on quality of the PS would potentially result in a better fit of model and data.

The vertical and horizontal movements as calculated by the different models are represented in Figure 22.

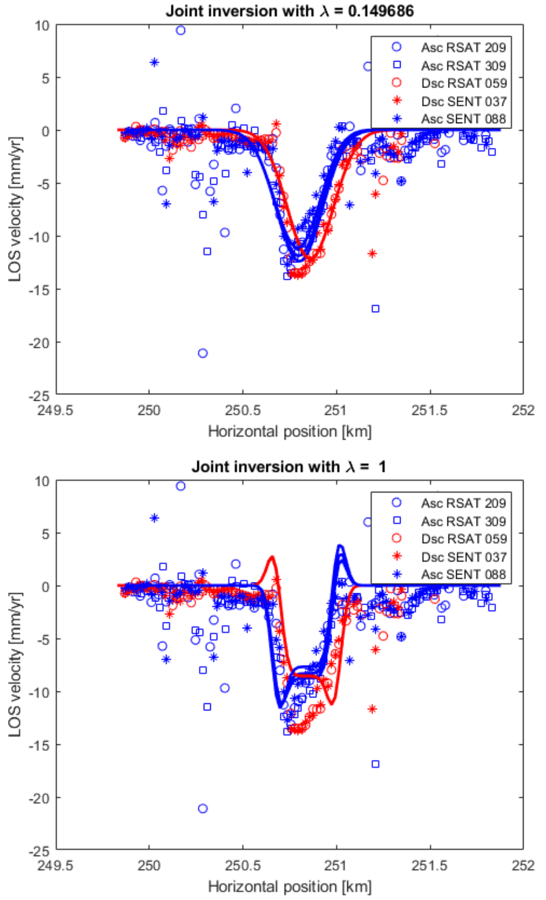

Figure 20. InSAR LOS data and model results along the EW line for both satellites (BJP models).

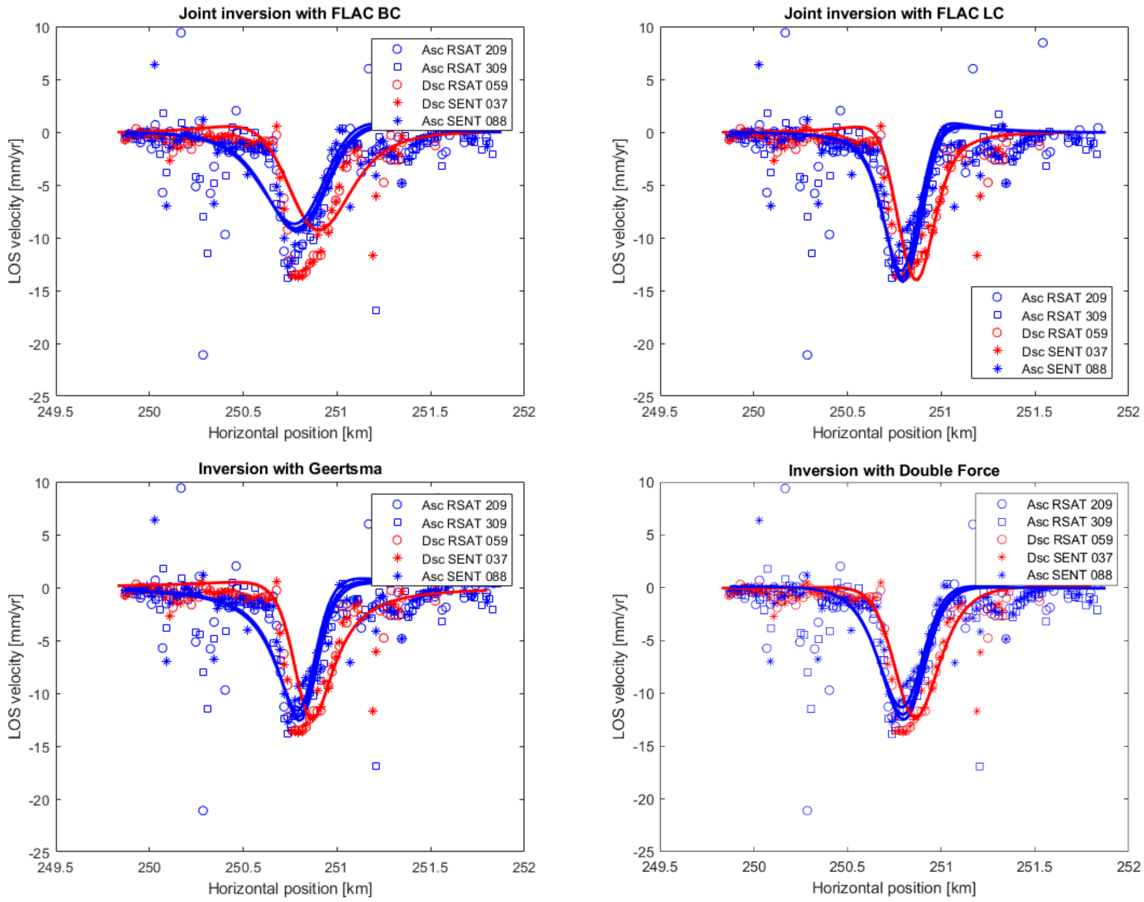

Figure 21. InSAR LOS data and model results along the EW line for both satellites (FLAC, Geertsma and Double Force models).

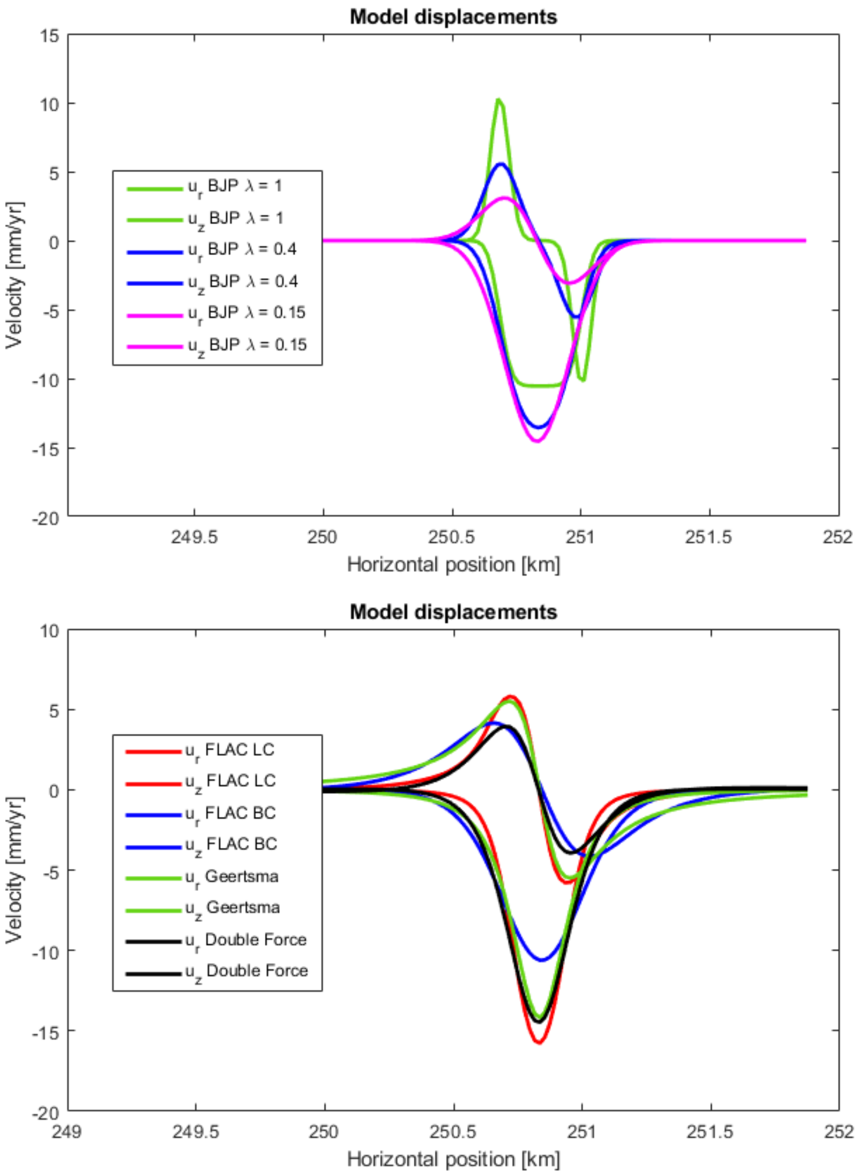

Figure 22. Vertical (z deformation (mm/y)) and horizontal (r) position (km) of the tested models along the EW line.

5. Conclusions

Salt mining activities in the Twente region induce surface deformation. With the withdrawal of salt, caverns develop in which the internal pressure is smaller than the virgin lithostatic stress. This results in limited subsidence at the surface. However, insufficient pressure management and suboptimal operations may lead to a substantial pressure drop and removal of the rocksalt roof above the cavern, increasing the likelihood of cavern instability, upward cavern migration and potential collapse, which in turn could cause significant surface deformation. Early detection of such instability is essential for mitigation. In this context, InSAR measurements constitute a valuable monitoring tool for the continuous observation of surface movements above active salt extraction sites.

During the project, we have evaluated four research questions and formulated answers to them.

1. **What are the quality control procedures of the InSAR data and what levels of accuracy and precision can be expected?**

InSAR uses phase information to extract surface deformation. In order to achieve a high precision, many other components influencing the interferometric phase need to be isolated, such as atmospheric noise. Additionally, only relative deformation with respect to a reference point is observed, meaning accuracy is dependent on the chosen reference. For temperate locations with vegetation and infrastructure, Persistent Scatterer Interferometry (PSI) is the best suitable methodology for InSAR-monitoring.

Typical quality control procedures of InSAR-data are focussed on ensuring that:

- Atmospheric corrections do not remove relevant signals from the data
- Reference point calibration can be validated with known in-situ data
- Scatterer positions are georeferenced properly

Many factors can influence the achieved precision, but the most relevant factors are the wavelength and the reflectivity of each (individual) scatterer. As a rule of thumb, the precision of each acquisition is better than 10% of the wavelength (< 3.1 mm for X-band, < 5.5mm for C-band). Pure PS-targets can reach a precision higher than 1 mm for both X-band and C-band. When using more than 60 SAR-images, the estimated linear trend for each scatterer is better than **1 mm/yr**.

For finding an accurate reference point, it is possible to calibrate the InSAR-results on GNSS benchmarks. However, these benchmarks are generally sparse and connecting them to InSAR-results can be challenging. Another approach is to use a statistical approach to calibrate the results on stable areas.

It should be noted that InSAR measurements are not pure measurements. In order to convert interferometric phase to deformation, many processing chains require a data-assimilation approach to retrieve model parameters and explain the signal. This process comes with assumptions on the expected signal, and the resulting measurements are therefore biased towards a selected model. In our view, the model used should be as simple as possible to avoid overfitting of noise patterns and to avoid biased measurements.

PS-InSAR results are inherently limited to locations that exhibit persistently strong and temporally stable. Consequently, surface modifications or infrastructural changes can disrupt phase coherence, leading to loss of measurable points and a reduction in spatial coverage. Sensar has found that on average, there is a 7% annual loss of PS-candidates. Therefore, long-term coverage can only be guaranteed by integrating change-detection techniques to enable the identification of scatterers that exhibit persistent coherence only over limited temporal intervals. We refer to these as 'robust scatterers' (RS-InSAR). This approach enhances point density over time and improves spatial coverage in regions undergoing surface or structural change.

Besides this, PSI-results are restricted to infrastructure and lack coverage on green areas. On vegetated areas, the observed phase values are influenced by moisture effects of the vegetation and the surface. With X-band and C-band, the signal stability (coherence) is insufficient to correct these effects. Although recent efforts have been made with complex data-assimilation, they heavily rely on the underlying model. It is still impossible to obtain reliable and independent InSAR-observations on vegetated surfaces. The increase in L-band sensors (NISAR, Rose-L, ALOS-4) is promising, as coherence on vegetated surfaces is expected to increase.

2. What are the global experiences with salt cavern monitoring using InSAR?

The literature review indicates that substantial knowledge exists regarding the behaviour of salt caverns and the conditions under which failure-related incidents may occur. Deformation within salt caverns typically progresses slowly and is primarily governed by the creep behaviour of rocksalt. However, deformation can also occur abruptly, particularly when triggered by operational or geomechanical incidents. The resulting spatial deformation patterns may therefore range from gradual subsidence to sudden, highly localized failures such as sinkhole formation.

Accurate information on cavern geometry, depth, and operational history is essential for assessing the likelihood and potential severity of incident-related deformation. Such information forms the basis for reliable risk assessments and supports effective monitoring and mitigation strategies.

Time-resolved InSAR monitoring of failure processes remains relatively uncommon, and even fewer studies establish a direct link between observed surface deformation and physical modelling of the underlying failure mechanisms. Although inverse modelling approaches have been applied in some cases, these efforts have predominantly focused on gradual, long-term deformation signals. Advancing the current state of knowledge requires the development and application of models capable of reproducing catastrophic failure processes and quantifying their expected surface displacement signatures. Such models are essential for improving the interpretation of InSAR observations and for assessing the potential impacts of sudden subsurface failures.

3. **Which locations over the last 10 years show subsidence rates which correspond to possible unstable salt caverns in Twente?**

The subsidence rates that we have established do not give reason to suspect unstable caverns in the Twenthe-Rijn region. This is in line with the studies instigated by Nobian (Reinvent GmBH, 2023, 2024a, 2024b, 2024c; Jakob, 2025). In this study we have shown that linear deformation hotspot and spatially correlated deformation pattern that correspond with known borehole locations can be detected.

Analysing InSAR data over the last 10 years, a subsidence hotspot is detected at the *Boortorenweg*. At this location severe cavern migration has taken place in the past and the signal observed is most likely a continuation of its post-collapse subsidence (stage 5 in Figure 6).

As deformation at the surface above the cavern is often slow, spatially correlated deformation patterns are considered relevant for potential cavern instability. Such spatial patterns are present at the *Beckumerstraat* in the Twente mining area, corresponding to borehole locations. This location may experience stronger deformation in the future and is recommended to be monitored for sudden changes in surface movement.

4. **What is the coupling between (known) Twente cavern deformation and subsidence data? Which Twente caverns may be unstable?**

There are various approaches to couple cavern deformation and subsidence with increasing levels of complexity. Caverns deformation is expected to appear in 5 stages (see Figure 6): convergence, deformation and migration, deflection of the top competent layer, collapse and consolidation. The first two stages are considered normal, during these stages limited surface deformation within the influence sphere is expected. As a rule of thumb, the sphere of influence is proportional to the depth of the cavern. During stages 3 and 4 a sinkhole forms, leading to an accelerated and more concentrated subsidence. Stage 5 is the aftermath of a collapse, resulting in further convergence and subsidence.

Therefore, the early detection of developing sinkholes is an important capability. We have demonstrated that such capability can be developed when applying modelling insights to advanced monitoring. In this sense, our contribution is an addition to the work of Chang and Hanssen (2014), who already showed the value of monitoring with interferometric radar and the identification of anomalies in temporal and spatial patterns for the early identification of upcoming sinkholes.

REinvent (2023) show that the process of cavern migration is slow – in the order of 10-15 mm/year. As a result, it will take more than a decade before the migration reaches unconsolidated layers and total failure occurs. Therefore, it seems sufficient to have yearly updates of the monitoring results for caverns which are prone to failure. With regard to InSAR this monitoring should focus on locations where surface movement is observed (e.g. more than 5 mm/year). Then the subsidence estimates can be scrutinized on their temporal behaviour: deeper investigations are appropriate when acceleration is observed. The PSI workflow that we deployed for the InSAR processing of the different satellite data has shown to be a powerful tool to follow the surface movement velocity as it evolves in time.

We have also demonstrated that it is possible to derive shape parameters from the data derived from ascending and descending tracks of the satellites. Our numerical analysis is limited, but it shows changes in the rate of surface movement when cavern collapse occurs, and it shows different spatial surface signatures for caverns who have migrated upwards from caverns who have not. When matching the shapes to the observed behaviour, a conclusion can be reached about the actual depth of the cavern. For the deformation pattern around the *Boortorenweg*, it showed that the depth of the converging volume was closer to 250 m than to 350 m, so this cavern had migrated upwards out of the rocksalt layers. Such analysis is therefore recommended for locations where surface movement rate accelerations are observed.

The BJP model did not represent the data well. Only with quite a small horizontal component of the displacement vector a reasonable match could be made. However, the characteristics of this match are unrealistic. A much better match was achieved with the integrated Double Force influence function. This function is actually based on physics. Even more, the match gave numbers for the source depth and radius in line with the known position and extent of the cavern.

Cavern characterization can be greatly helped with inverting surface movement estimates obtained with InSAR. The temporal behaviour can be analysed to identify changes in the deformation rate, which may be indicative for cavern migration. The shape attributes show the depth and areal extent of the cavern. Their temporal behaviour can be a strong piece of information for the identification of failure.

In this project we have shown that InSAR can be a powerful monitoring tool for early detection of abnormal surface deformations in region of salt caverns. The surface deformations observed with InSAR are in good agreement with geomechanical modelling results, taking into account subsurface characteristics and cavern geometry.

From the research conducted it becomes evident that a good monitoring strategy, tailored to the specific region of interest is essential. InSAR can serve as an early detection of abnormal surface deformation, but local expertise of the region and type of caverns is needed to set appropriate detection thresholds. To scale up monitoring, inversion with geomechanical modelling can provide more details regarding instability of caverns. This requires expert knowledge on modelling and geophysical properties of the region and caverns.

Our analysis highlights the importance of spatial coverage in the InSAR data. For monitoring of deformation signals one should aim for the best coverage possible. Limiting factors in this regard are the presence of vegetation (e.g. rural areas) and spatial resolution of the satellite. As each available radar satellite mission has its own specifications, a trade-off is to be done between spatial coverage and temporal baseline. A long temporal baseline is preferred in order to detect changes and receive a detailed progression of the movement over time, but our research points out that spatial coverage is even more important. Additionally, the ability to correct for local changes on the ground (e.g. construction sites), including RS estimates, increases the availability of scatterers in areas with many changes.

With these conclusions made, we also recommend a follow-up study with L-band datasets, as they have a high potential for overcoming the lack of coverage in vegetated areas.

6. References

Bérest, P. &. (2003). Safety of salt caverns used for underground storage blow out; mechanical instability; seepage; cavern abandonment. *Oil & Gas Science and Technology, 58(3)*, 361-384.

Bérest, P. (2017). Cases, causes and classifications of craters above salt caverns. *International Journal of Rock Mechanics and Mining Sciences, 100*, 318-329.

Bérest, P. e. (2023). *Risk assessment of hydrogen storage in a conglomerate of salt caverns in the Netherlands. KEM-28 Final Report.* KEM.

Bérest, P. R. (2019). Review and analysis of historical leakages from storage salt caverns wells. *Oil & Gas Science and Technology–Revue d'IFP Energies nouvelles, 74*, 27.

Chang, L. H. (2014). Detection of cavity migration and sinkhole risk using radar interferometric time series. *Remote sensing of environment, 147*, 56-64.

Eising, J. (2021). *Risk analysis of worldwide cavern storage.* MSc Thesis, University of Amsterdam.

Even, M. W. (2020). Complex surface displacements above the storage cavern field at Epe, NW-Germany, Observed by Multi-Temporal SAR-interferometry. *Remote sensing, 12(20)*, 3348.

Ferretti, A. (2014). *Satellite InSAR data: reservoir monitoring from space.* EAGE.

Fibbi, G. L. (2025). Open-Source InSAR Data to Detect Ground Displacement Induced by Underground Gas Storage Reservoirs. *Earth Systems and Environment*, 1-18.

Fokker, P. A. (2002). Salt deformation and subsidence. *J. Learned and Applied Soil Mechanics, 22*, 57.

Fokker, P. A. (2016). Application of an ensemble smoother with multiple data assimilation to the Bergermeer gas field, using PS-InSAR. *Geomechanics for Energy and the Environment, 5*.

Fokker, P. A. (2018). On the use of influence functions for subsidence evaluation. *In ARMA US Rock Mechanics/Geomechanics Symposium. American Rock Mechanics Association.*

Fokker, P. C. (2025). Subsidence. In J. V.-J. Ten Veen, *Geology of the Netherlands* (2 ed., pp. 825-847). Amsterdam University Press. doi:10.5117/9789463728362_ch23

Furst, S. L. (2021). Monitoring surface deformation of deep salt mining in Vauvert (France), combining InSAR and leveling data for multi-source inversion. *Solid Earth, 12*(1), 15-34.

Gao, H. L. (2025). Observation and evaluation of surface and underground space changes in well salt mining based on InSAR: a case study of Qingjiang salt mine, Zhangshu, China. *International Journal of Digital Earth, 1*.

Geertsma, J. (1973). Land subsidence above compacting oil and gas reservoirs. *Journal of petroleum technology, 25(06)*, 734-744.

Groenenberg, R. D. (2025). Salt Production. In J. V.-J. Ten Veen, *Geology of the Netherlands* (2 ed., pp. 603-625). Amsterdam University Press.

Hanssen, R. F. (2001). *Radar interferometry: data interpretation and error analysis* (Vol. 2). Springer Science & Business Media.

Hunfeld, L. B. (2022). The influence of a threshold stress for pressure solution creep on cavern convergence and subsidence behavior–An FEM study. CRC Press.

Jakob, C. P. (2025). The Bekendam-Jakob-Pinkse (BJP) subsidence prognosis algorithm for migrating salt caverns in a bedded salt deposit near Hengelo, The Netherlands. *SMRI Spring 2025 Technical Conference.* Wilhelmshaven.

Janna, C. C. (2012). A geomechanical transversely isotropic model of the Po River basin using PSInSAR derived horizontal displacement. *International Journal of Rock Mechanics and Mining Sciences, 51*, 105-118.

Liu, X. X. (2019). Mining-induced time-series deformation investigation based on SBAS-InSAR technique: A case study of drilling water solution rock salt mine. *Sensors, 19*(4), 5511.

Malinowska, A. G. (2018). Mapping of slow vertical ground movement caused by salt cavern convergence with sentinel-1 tops data. *Archives of Mining Sciences*.

Menke, W. (2018). *Geophysical data analysis: Discrete inverse theory* (4 ed.). Academic press.

Meyer, F. &. (2006). *Methods for Atmospheric Correction in INSAR Data.*

Mogi, K. (1958). Relations between the eruptions of various volcanoes and the deformations of the ground surfaces around them. *Bulletin of the Earthquake Research Institute, 36*(99), 134.

Montalti, R. F. (2023). Energy Storage in Salt Caverns: the Role of Insar Monitoring. *In The Fourth EAGE Global Energy Transition Conference and Exhibition. European Association of Geoscientists & Engineers.*, *2023-1*, pp. 1-5.

Okada, Y. (1992). Internal deformation due to shear and tensile faults in a half-space. *Bulletin of the seismological society of America, 82*(2), 1018-1040.

Parwata, I. N. (2020). Monitoring the subsidence induced by salt mining in Tuzla, Bosnia and Herzegovina by SBAS-DInSAR method. *Rock mechanics and rock engineering*, 1-21.

REinvent GmBH . (2024b). *Update Migration Study Twenthe-Rijn Phase 1. Report Part 3 – Validation of the BJP-Algorithm by assessment of historical migration behaviour of selected TWR caverns and determination of the likelihood of migration.*

REinvent GmBH. (2023). *Update Migration Study Twenthe-Rijn Phase 1. Report Part 1 – Fundamental principles used in reconstruction.*

REinvent GmBH. (2024a). *Update Migration Study Twenthe-Rijn Phase 1. Report Part 2 – The Bekendam-Jakob-Pinkse (PKJ) subsidence prognosis algorithm for migrating salt caverns in a bedded stratigraphy.*

REinvent GmBH. (2024c). *Update Migration Study Twenthe-Rijn Phase 1. Report Part 4 – Subsidence predictions for potential future migration and recommendations on mitigative action by means of backfillin.*

Rucker, M. L. (2013). Using InSAR to detect subsidence at brine wells, sinkhole sites, and mines. *Carbonates and Evaporites, 28*(1), 141-147.

Sroka, A. M. (2017). Forecast of rock mass and ground surface movements caused by the convergence of salt caverns for storage of liquid and gaseous energy carriers. *GEOKINEMATISCHER TAG.* Freiberg.

Tajduś, K. S. (2021). Surface deformations caused by the convergence of large underground gas storage facilities. *Energies, 14*(2), 402.

Tarantola, A. (2005). Inverse problem theory and methods for model parameter estimation. *Society for industrial and applied mathematics*.

Torres, R. S. (2012). GMES Sentinel-1 mission. *Remote sensing of environment, 120*, 9-24.

Vasco, D. R. (2010). Satellite-based measurements of surface deformation reveal fluid flow associated with the geological storage of carbon dioxide. *Geophysical Research Letters, 37*(3).

Verberne, M. K. (2025). Disentangling subsidence from shallow soil processes and gas extraction in a Dutch UNESCO World Heritage polder with InSAR and data assimilation.

Wang, Z. L. (2024). Geothermal Energy Extraction–Induced Ground Movement Monitoring by InSAR and Its Implication for Reservoir Management. *ournal of Energy Engineering, 150*(5).

Yan, T., & Burbey, T. J. (2008). The value of subsidence data in ground water model calibration. *Groundwater, 46*(4), 538-550.

Yang, C., & Wang, T. (2024). Safety Monitoring Technology and Its Engineering Application for Salt Cavern Underground Gas Storage. In *Underground Rock Salt Used for Energy Storage: Theory and Engineering Practice* (pp. 431-497). Singapore: Springer Nature.

Yang, C., Jing, W., Daemen, J. J., Zhang, G., & Du, C. (2013). Analysis of major risks associated with hydrocarbon storage caverns in bedded salt rock. *Reliability Engineering & System Safety, 113*, 94-111.

Appendix A InSAR results at *Boortorenweg*

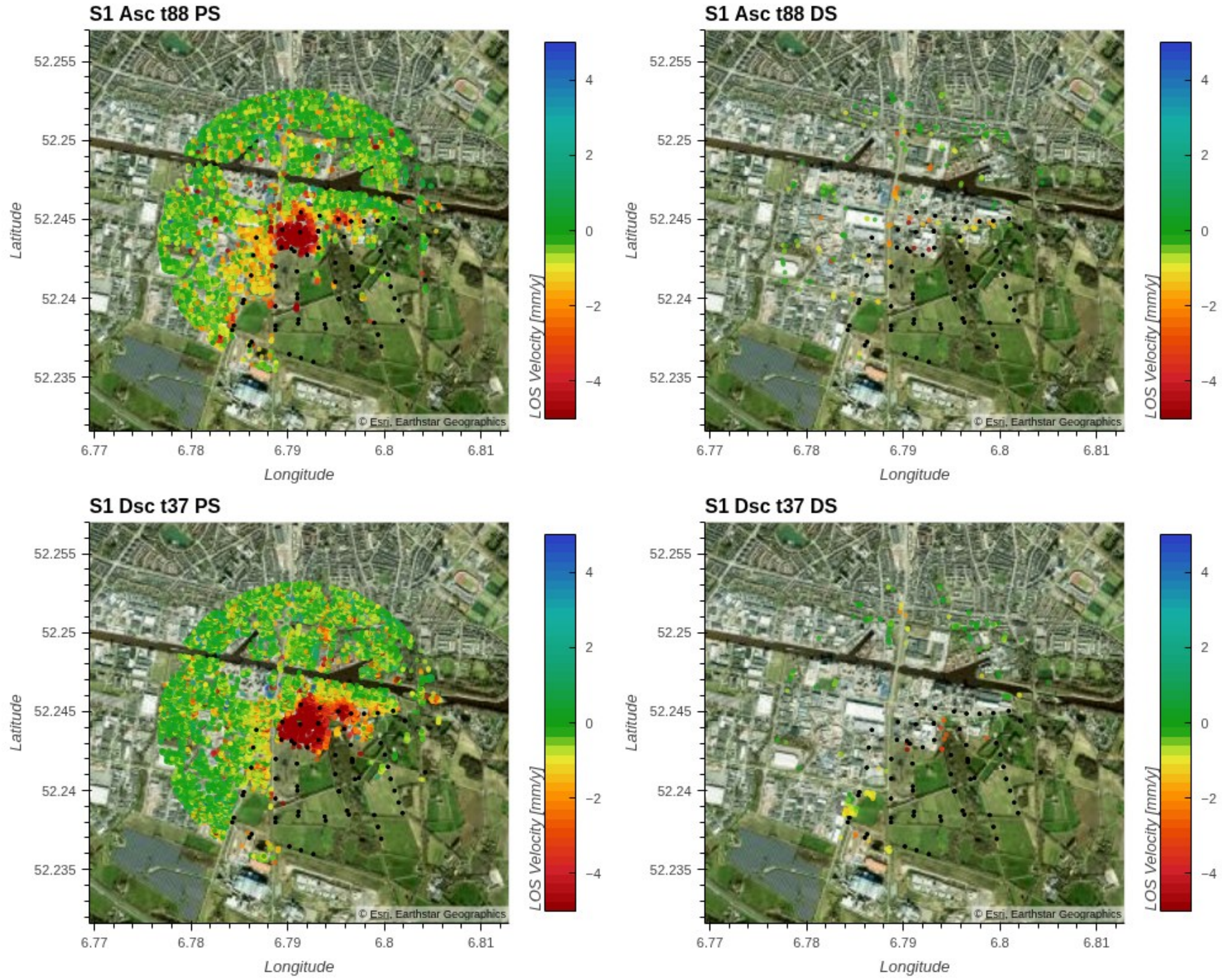

Figure 23. Sentinel 1 InSAR LOS results for two stacks of track 37 and track 88, PS and DS. For these results a correction has been applied for the atmosphere (with APS). Black dots are borehole locations.

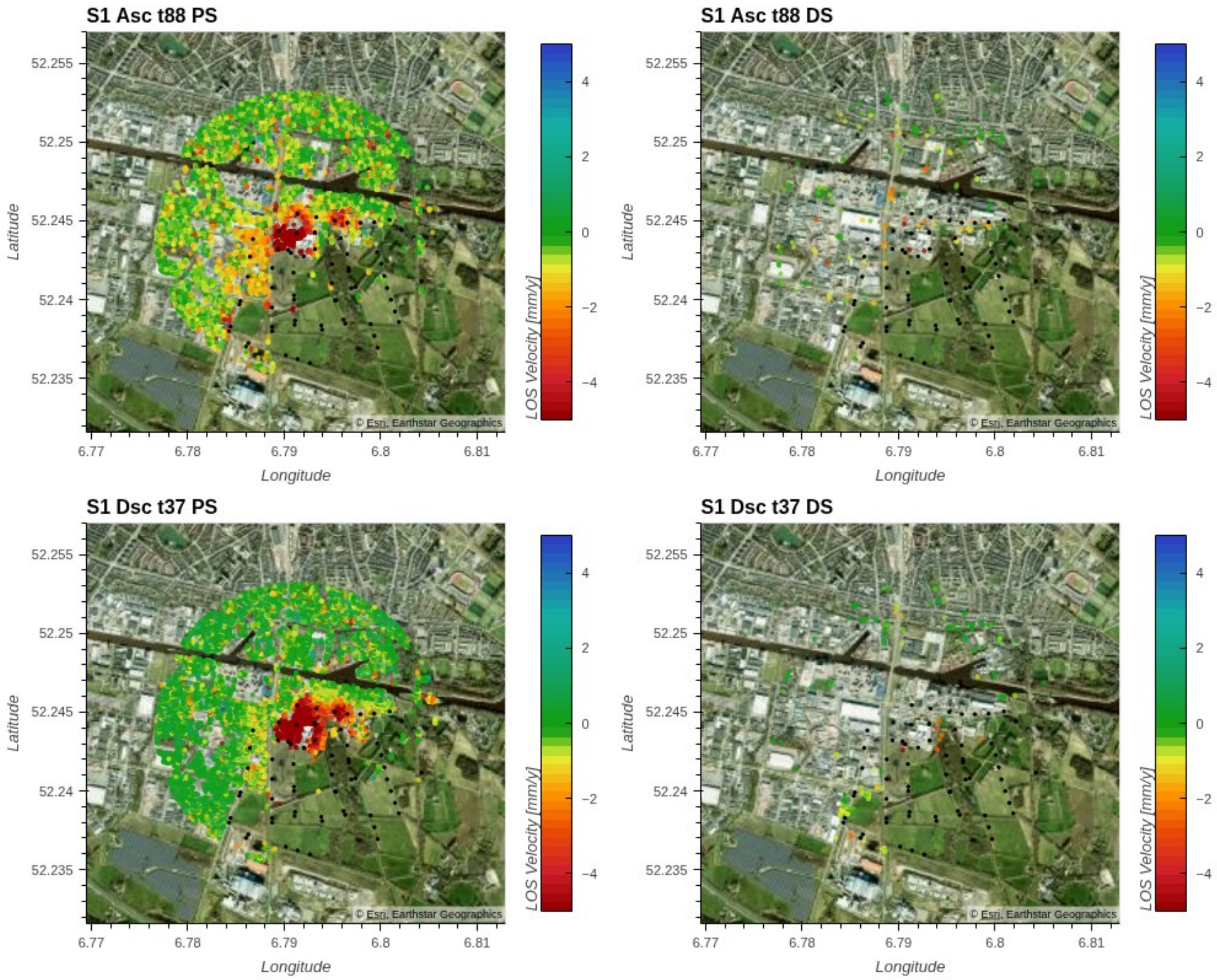

Figure 24. Sentinel 1 InSAR LOS results for two stacks of track 37 and track 88, PS and DS. For these results no correction has been applied for the atmosphere (without APS).Black dots are borehole locations.

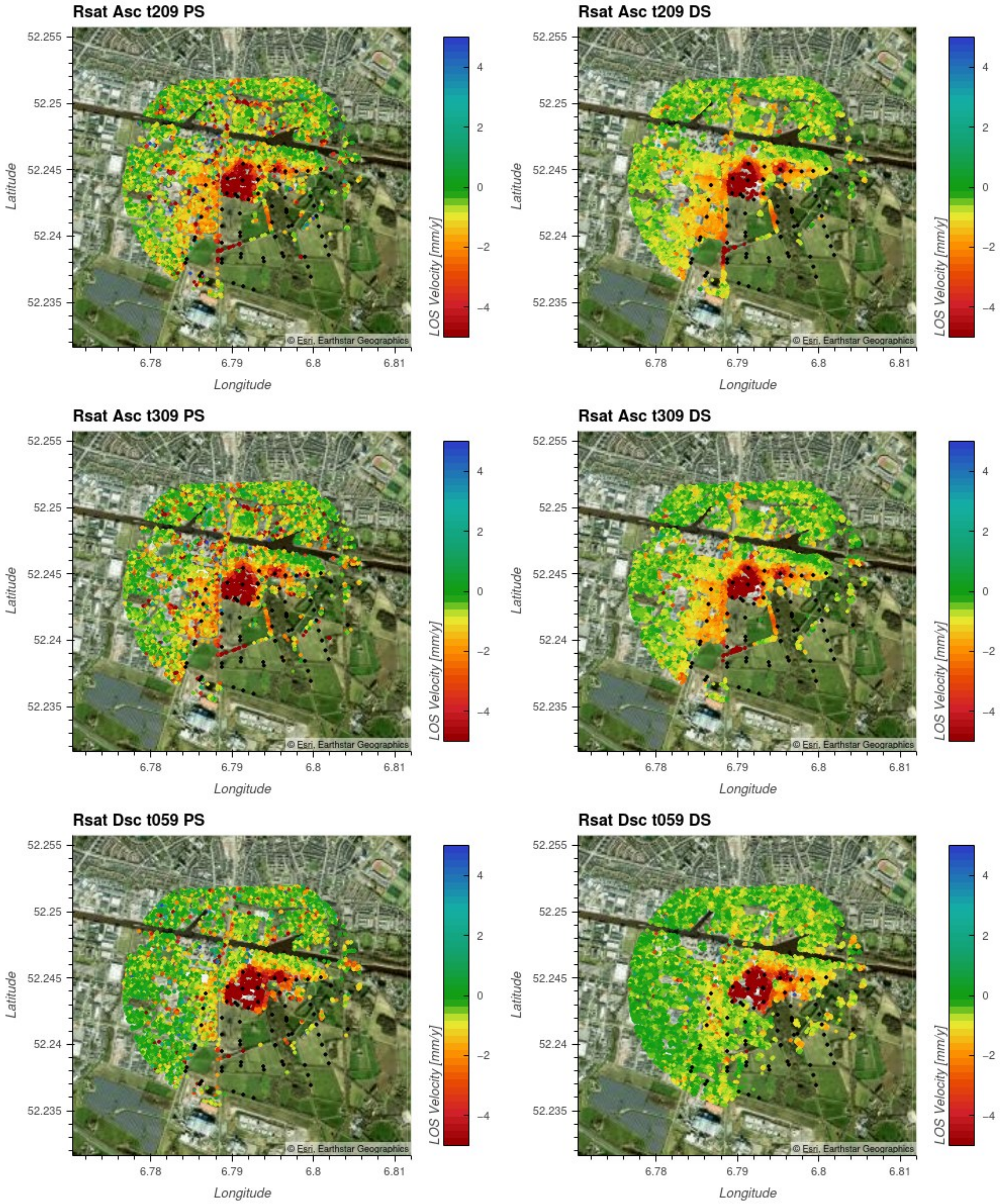

Figure 25. RadarSAT-2 LOS InSAR results for three stacks of tracks 209, 309 and 59, PS and DS. For these results a correction has been applied for the atmosphere (with APS).

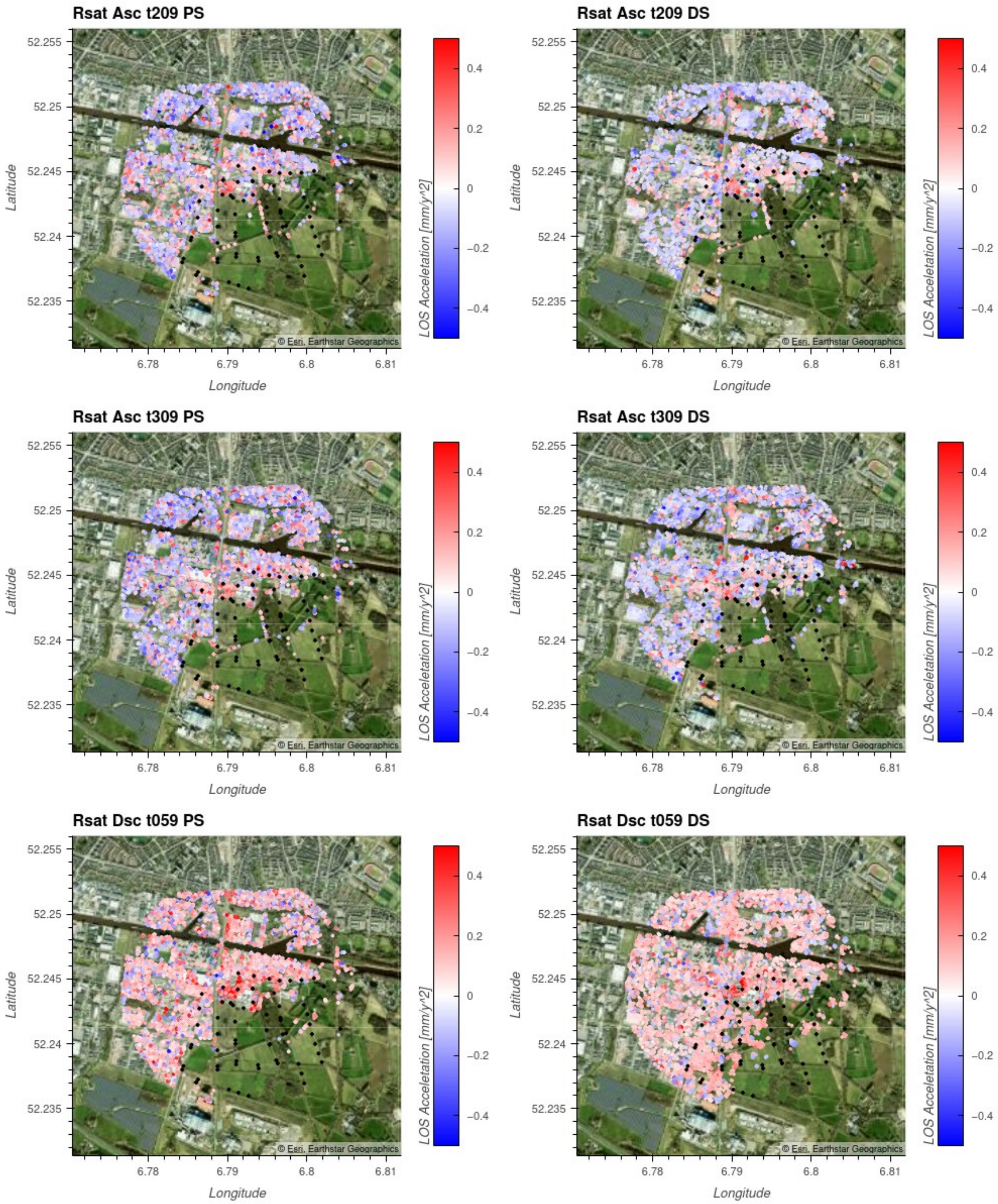

Figure 26. Quadratic model component (mm/yr²) of RadarSAT-2 LOS InSAR results for three stacks of tracks 209, 309 and 59, PS and DS. For these results a correction has been applied for the atmosphere (with APS).

Appendix B InSAR results around Beckumerstraat

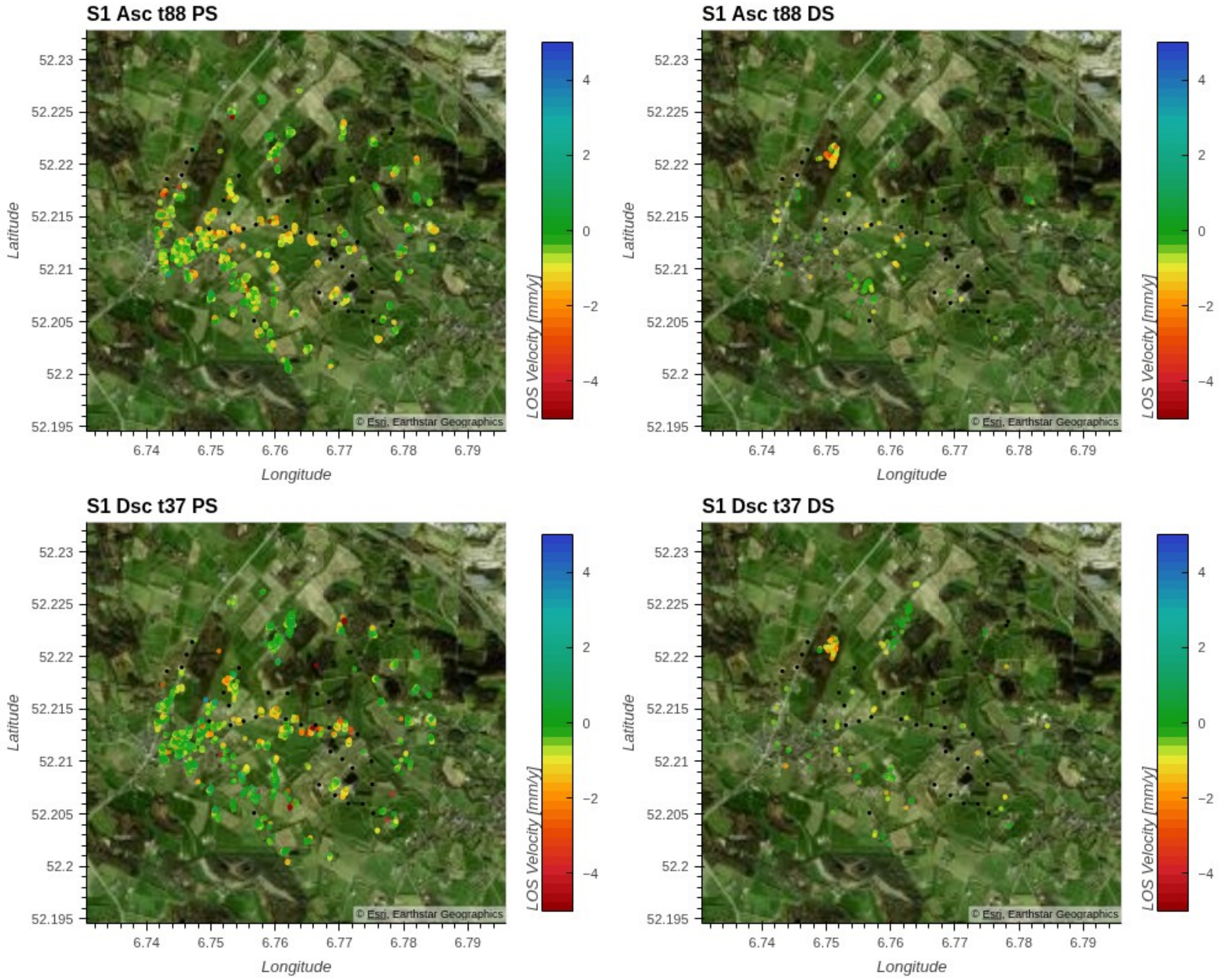

Figure 27. Sentinel 1 InSAR LOS results for two stacks of track 37 and track 88, PS and DS at Beckumerstraat. Correction of atmosphere has been applied (with APS). Black dots are borehole locations.

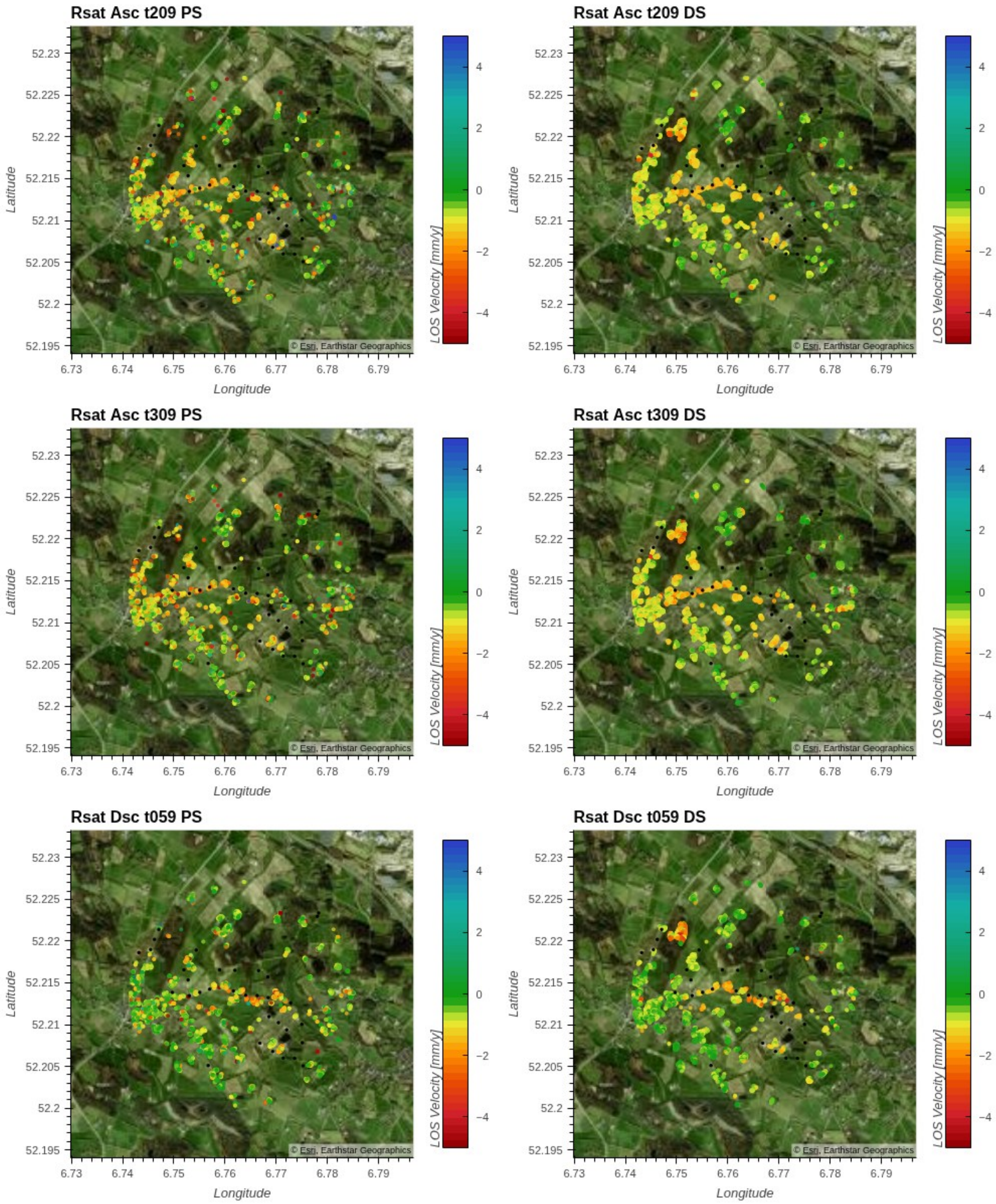

Figure 28. RadarSAT-2 InSAR LOS results for three stacks of tracks 209, 309 and 59, PS and DS at Beckumerstraat. Correction has been applied for the atmosphere (with APS). Black dots are borehole locations.

Appendix C InSAR results at *Zouthuisje*

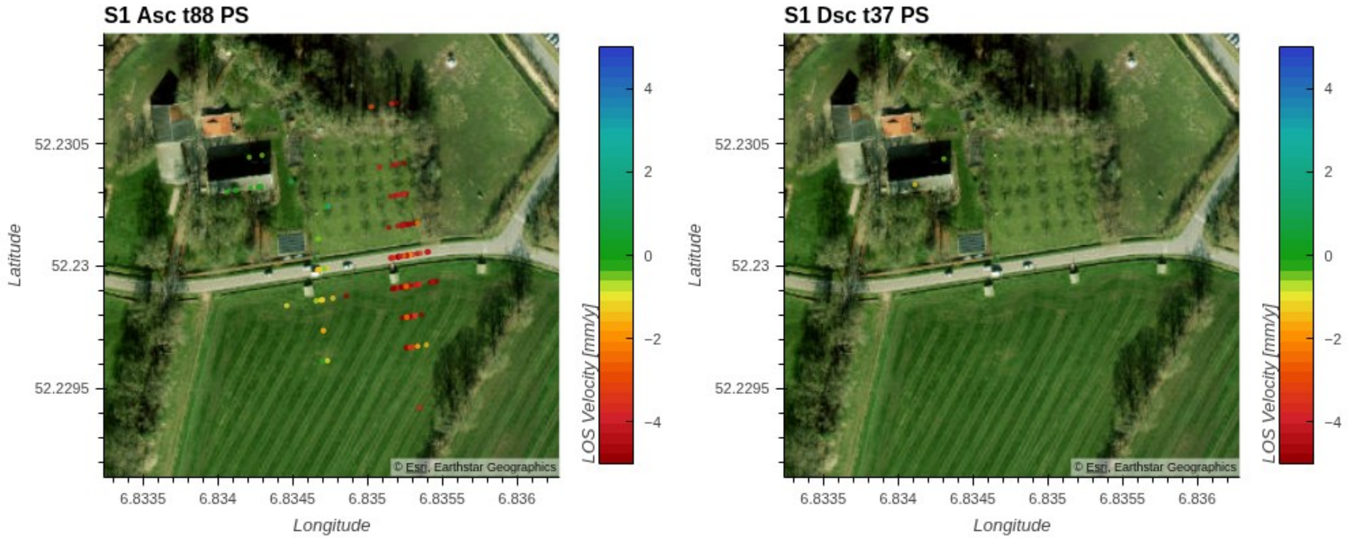

Figure 29. Sentinel-1 PS and DS InSAR LOS results for the asc (track 88) and dsc (track37) stack at the Zouthuisje location. Correction has been applied for atmosphere (with APS).

Appendix D Model results at *Boortorenweg*

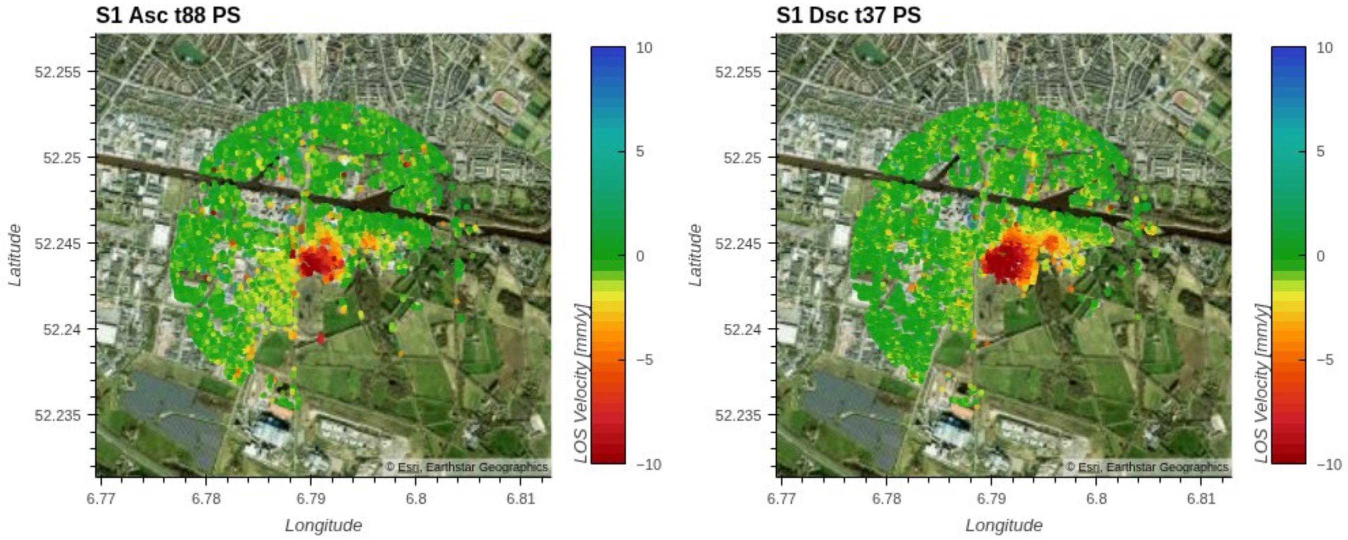

Figure 30. InSAR LOS data on which the model inversions are based: Sentinel-1 PS for the descending (T37) and ascending (T88) track at the Boortorenweg. EPSG: 4326.

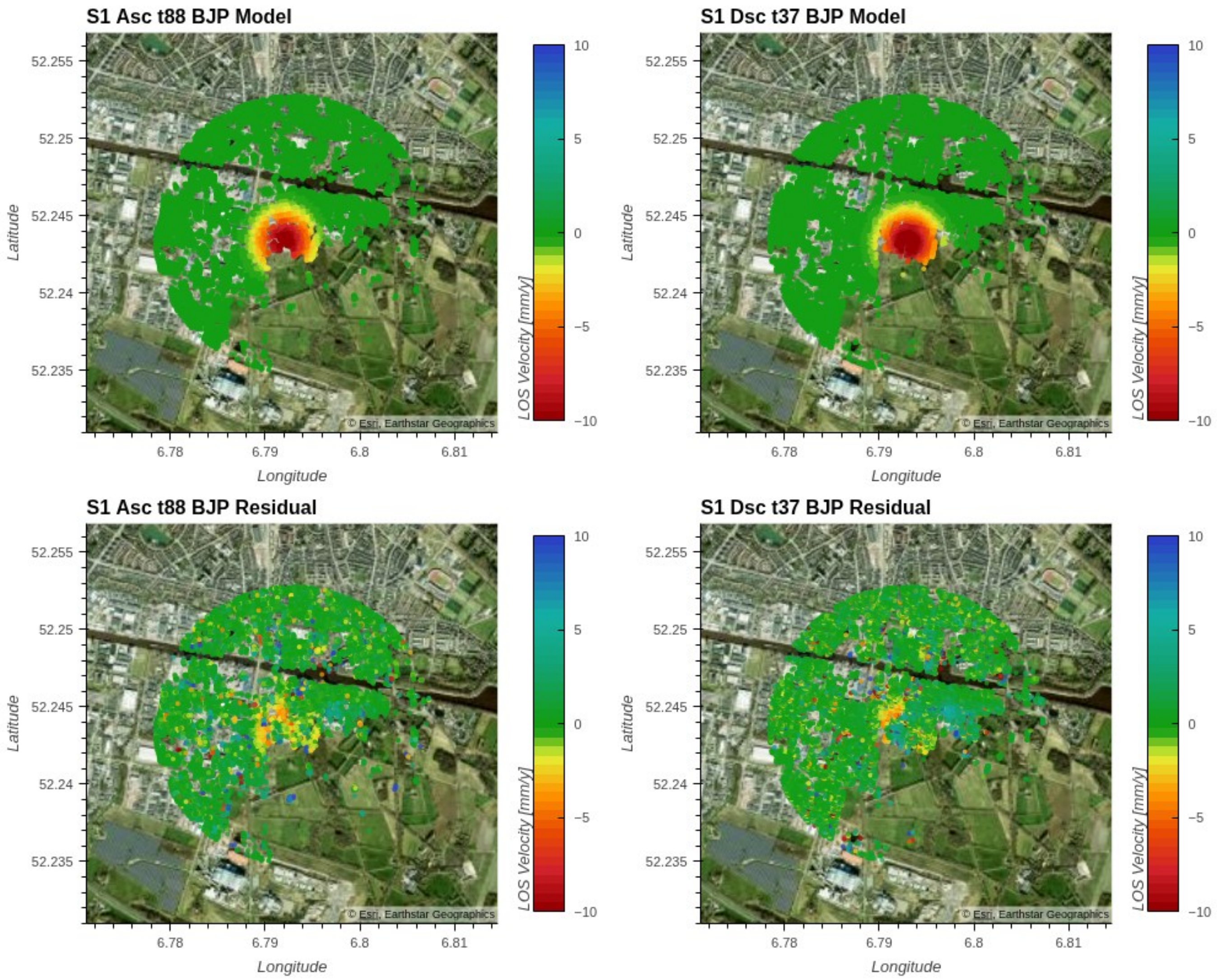

Figure 31. Model inversion results (top) and residual (bottom) for both tracks using the LOS Sentinel-1 data with the BJP model and optimized λ. Units are in mm/y. Red indicated subsidence blue uplift in the model plots. Red indicates negative residuals. EPSG: 4326.

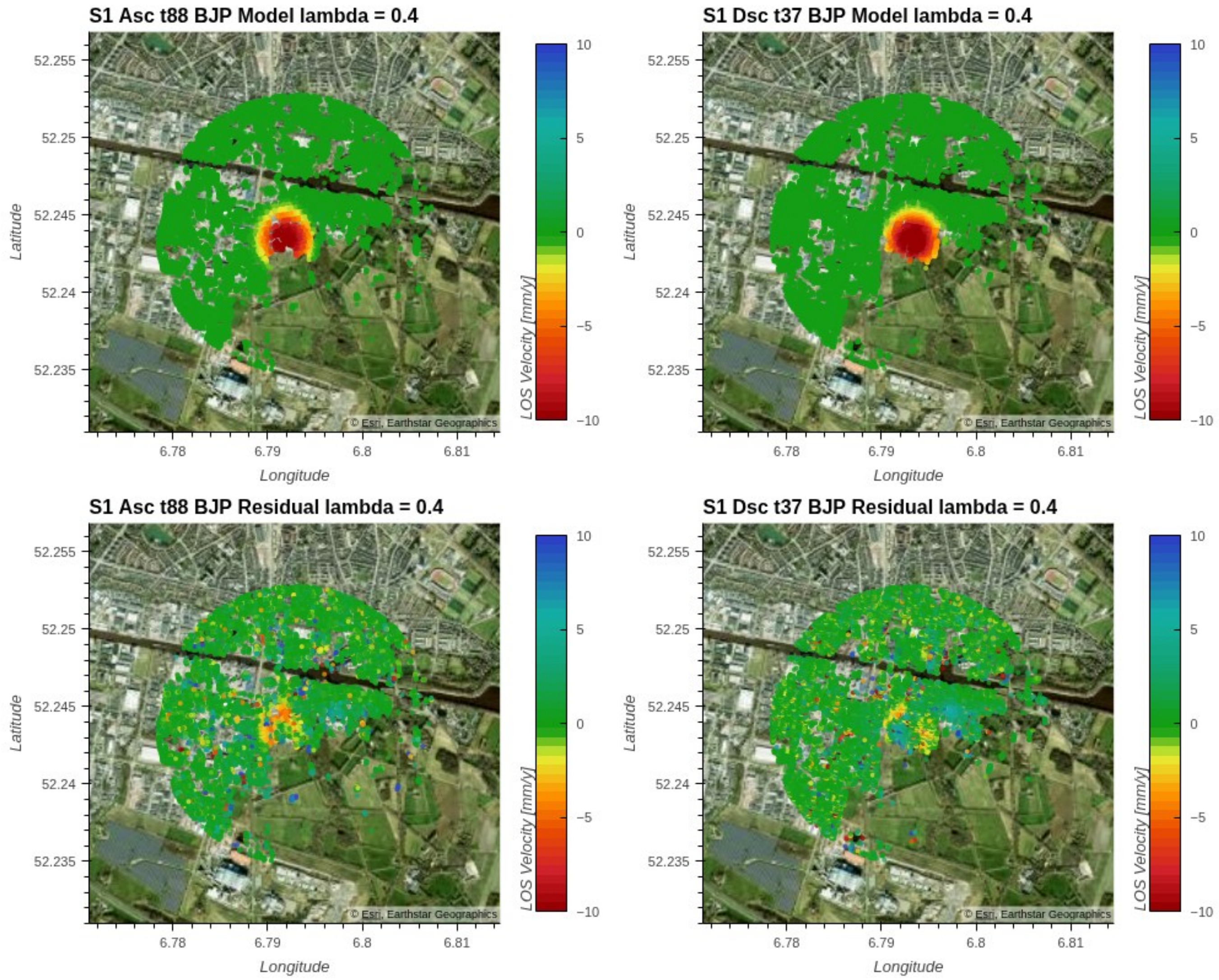

Figure 32. Model inversion results (top) and residuals (bottom) for both tracks using the LOS Sentinel-1 data with the BJP model and fixed λ=0.4. EPSG: 4326.

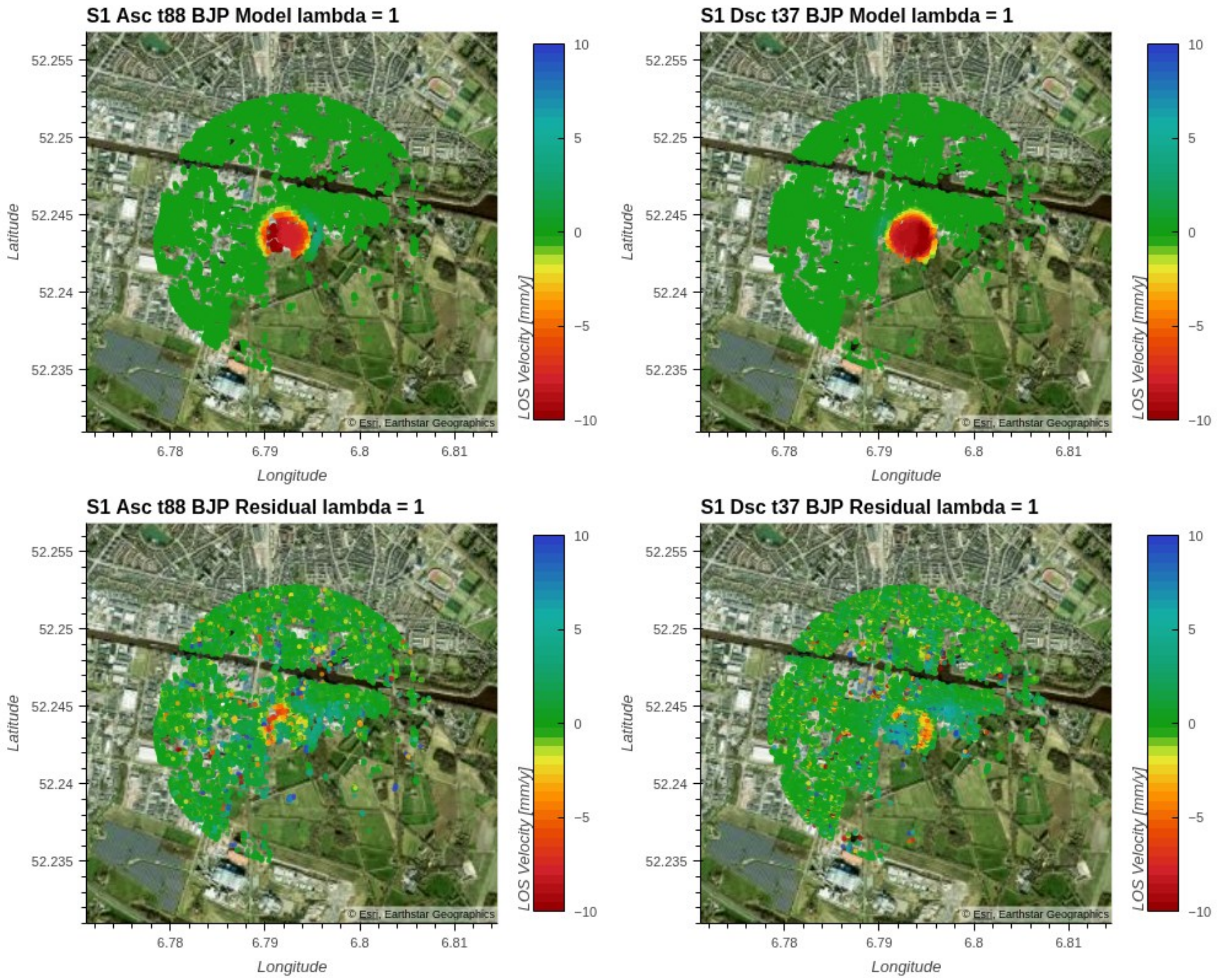

Figure 33. Model inversion results (top) and residuals (bottom) for both tracks using the LOS Sentinel-1 data with BJP model and fixed λ=1. EPSG: 4326.

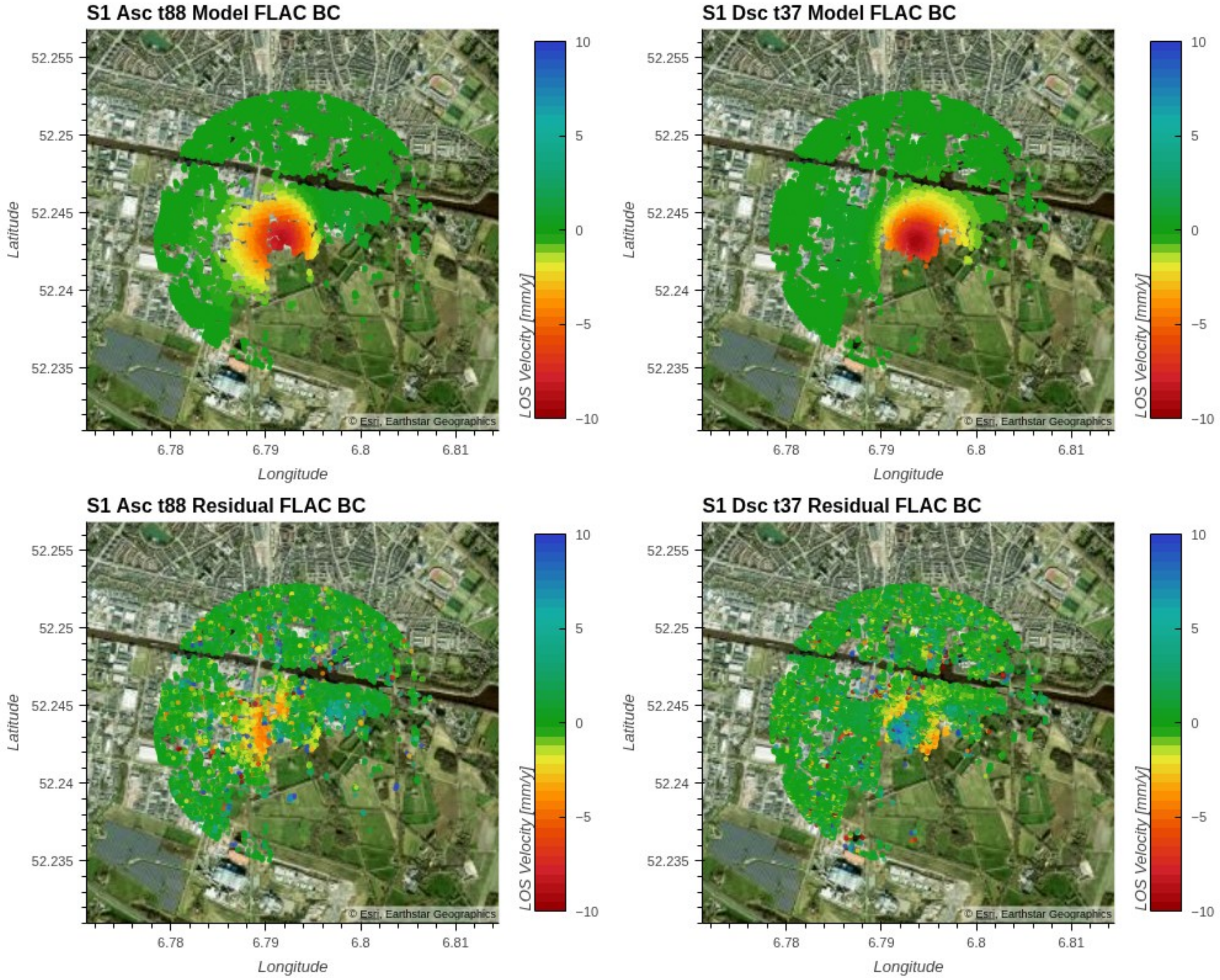

Figure 34. Model inversion results (top) and residuals (bottom) for both tracks using the LOS Sentinel-1 data with Base Case FLAC model. EPSG: 4326.

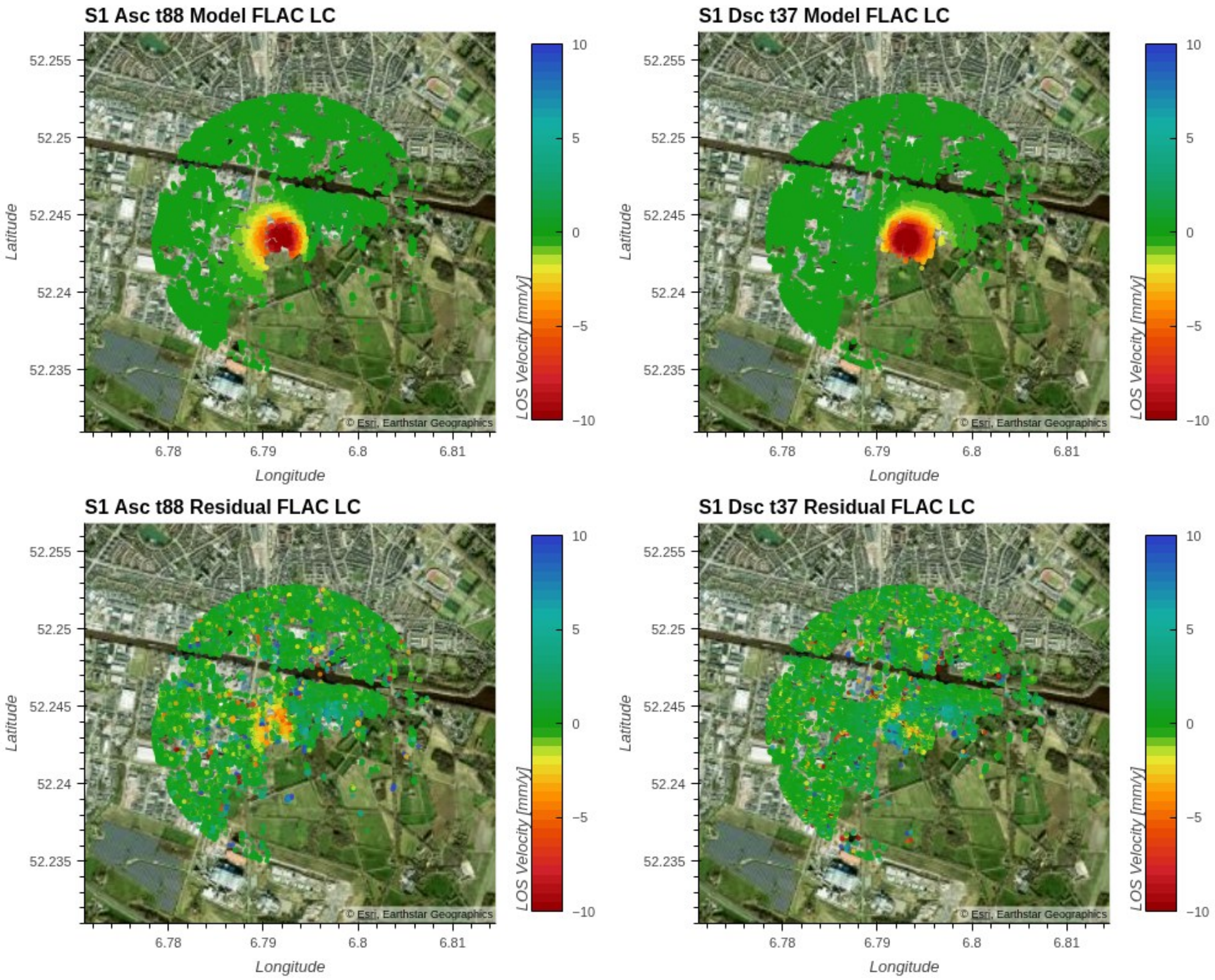

Figure 35. Model inversion results (top) and residuals (bottom) for both tracks using the LOS Sentinel-1 data with FLAC model with large cavern. EPSG: 4326.

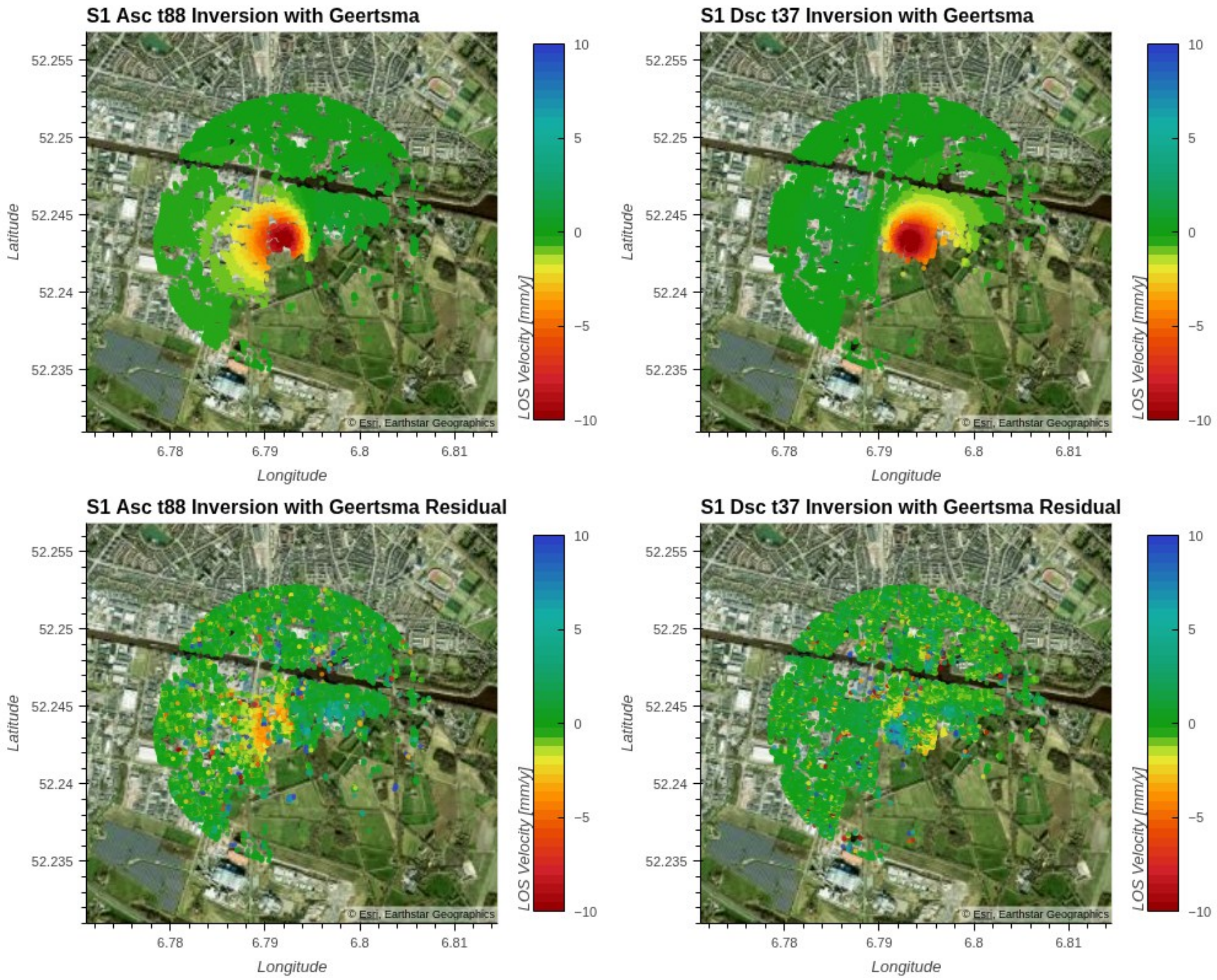

Figure 36. Model inversion results (top) and residuals (bottom) for both tracks using the LOS Sentinel-1 data with Geertsma model. EPSG: 4326.

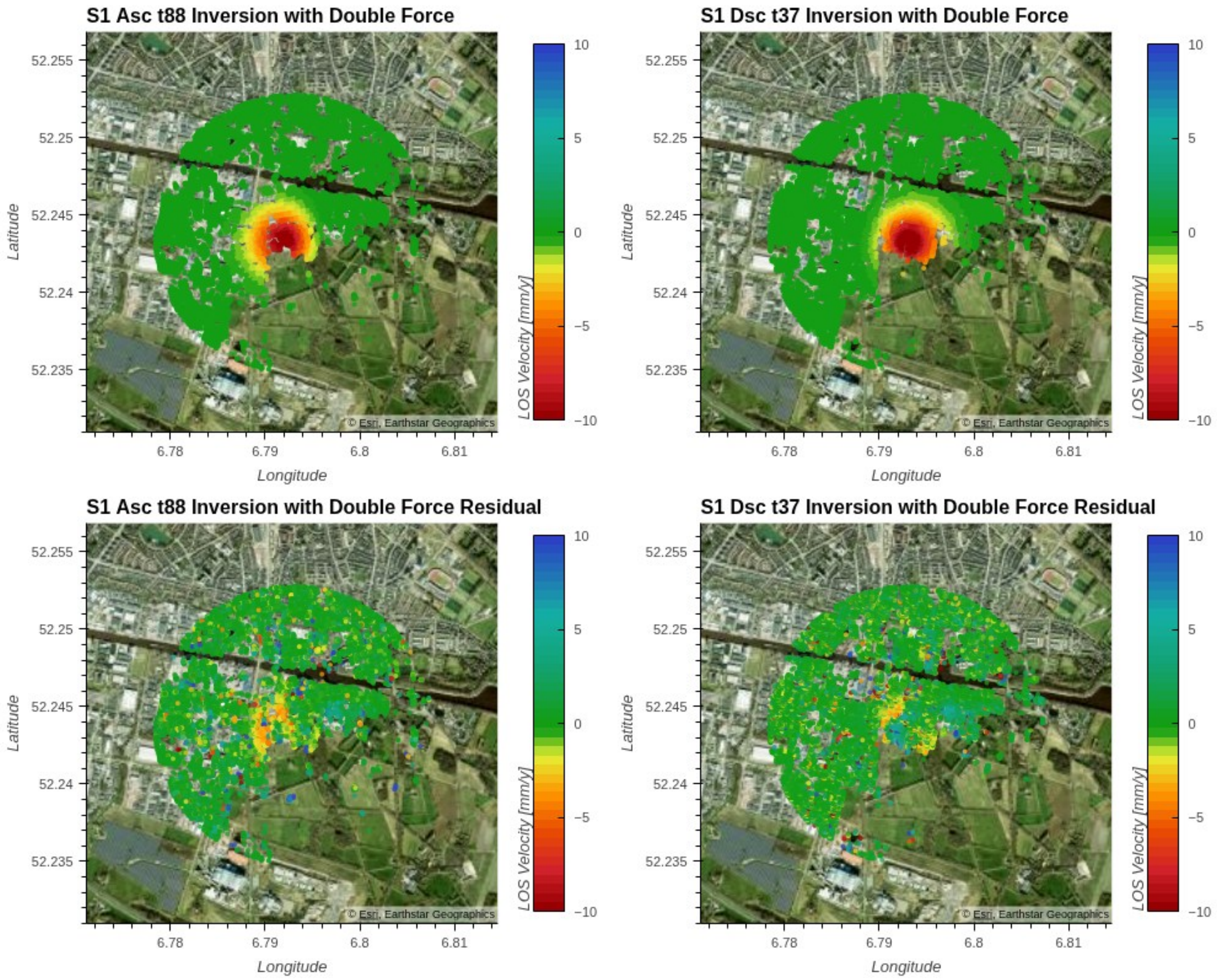

Figure 37. Model inversion results (top) and residuals (bottom) for both tracks using the LOS Sentinel-1 data with Double Force model. EPSG: 4326.

Appendix E Analytical Influence Functions

The Gaussian influence function is given by

$$u_z^{Gauss}(r) = u_{max} \cdot \exp\left(-\pi \frac{r^2}{R_{Sroka}^2}\right)$$
$$u_r^{Gauss}(r) = \lambda R_{Sroka} \cdot \frac{du_z}{dr} = -\frac{2\pi r\lambda}{R_{Sroka}} \cdot u_{max} \cdot \exp\left(-\pi \frac{r^2}{R_{Sroka}^2}\right) \quad \text{Eq. 6}$$

Replacing R_{Sroka} by $0.5 \cdot R$ we have the Gaussian function underlying the BJP (Bekendam-Jakob-Pinkse) solution

$$u_z^{Gauss}(r) = u_{max} \cdot \exp\left(-\pi \frac{4r^2}{R^2}\right)$$
$$u_r^{Gauss}(r) = \frac{\lambda R}{2} \cdot \frac{du_z}{dr} = -\frac{4\pi r\lambda}{R} \cdot u_{max} \cdot \exp\left(-\pi \frac{4r^2}{R^2}\right) \quad \text{Eq. 7}$$
$$r = \sqrt{(x - x_c)^2 + (y - y_c)^2}$$

In this equation, r is determined with respect to the position of the source. (x_c, y_c). For a laterally extended source, we integrate this expression over a square with dimensions $2r'$ around point $(0,0)$, and we choose the position on the surface on a line from the center of the square in the x-direction, $y = 0$. Further, we substitute $\frac{u_{max}R^2}{8} = \frac{S}{2}$ and we obtain the BJP solution with the addition of the horizontal movement:

$$u_z^{BJP}(x, y = 0) = u_{max} \int_{-r'}^{r'} \int_{-r'}^{r'} \exp\left(-4\pi \frac{(x - x_c)^2 + y_c^2}{R^2}\right) dx_c dy_c =$$
$$= \frac{S}{2} \operatorname{erf}\left(\frac{\sqrt{4\pi} \cdot r'}{R}\right) \times \left[\operatorname{erf}\left(\frac{\sqrt{4\pi} \cdot (r' + x)}{R}\right) + \operatorname{erf}\left(\frac{\sqrt{4\pi} \cdot (r' - x)}{R}\right)\right] \quad \text{Eq. 8}$$
$$u_r^{BJP}(x, y = 0) = \lambda S \operatorname{erf}\left(\frac{\sqrt{4\pi} \cdot r'}{R}\right) \times \left[\exp\left(-\frac{4\pi \cdot (r' + x)^2}{R^2}\right) - \exp\left(-\frac{4\pi \cdot (r' - x)^2}{R^2}\right)\right]$$

A peculiar property of this solution is that the integral is taken over a square source, but the solution is assumed to be radially symmetric. The background of this choice is that the integral is now analytically possible and the mismatch with the full 2D radially symmetric solution is small. The main characteristics are the far-field behaviour and the solution above the edge of the areal source.

We can follow the same procedure for Geertsma's source and for the Double Force source. The Centre of Compression (Geertsma) source and the Double Force source are given by the functions

$$u_{z,Geertsma}(x, y) = \frac{1 - \nu}{\pi} \cdot \frac{D}{R^3}$$
$$u_{x,Geertsma}(x, y) = \frac{1 - \nu}{\pi} \cdot \frac{x}{R^3}$$
$$u_{z,DF}(x, y) = \frac{1 - \nu}{\pi(2 - 4\nu)} \cdot D \cdot \left\{\frac{2\nu}{R^3} - \frac{3D^2}{R^5}\right\} \quad \text{Eq. 9}$$
$$u_{x,DF}(x, y) = \frac{1 - \nu}{\pi(2 - 4\nu)} \cdot x \cdot \left\{\frac{2\nu}{R^3} - \frac{3D^2}{R^5}\right\}$$
$$R = \sqrt{x^2 + y^2 + D^2}$$

We integrate those in the same manner:

$$u_{z,r}^{sq}(x, y = 0) = \int_{-r'}^{r'} \int_{-r'}^{r'} u(x - x_c, y_c)\ dx_c dy_c \quad \text{Eq. 10}$$
$$= P(u)(r', r') - P(u)(r', -r') - P(u)(-r', r') + P(u)(-r', -r')$$

Here, the double primitive $\boldsymbol{P}(\boldsymbol{f})$ for a function f is given by $\boldsymbol{P}(\boldsymbol{f})(\boldsymbol{x}, \boldsymbol{y}) = \int\int \boldsymbol{f}(\boldsymbol{x}, \boldsymbol{y})dxdy$. Primitives for the various functions in Eq. 9 are given by

$$P\left(\frac{1}{R^3}\right) = -\frac{1}{c}\arctan\frac{xy}{cR}$$
$$P\left(\frac{x}{R^3}\right) = -\log(y+R)$$
$$P\left(\frac{1}{R^5}\right) = \frac{1}{3c^3}\arctan\frac{xy}{cR} + \frac{1}{3c^2}\left\{\frac{xy}{(y^2+c^2)R} + \frac{xy}{(x^2+c^2)R}\right\}$$
$$P\left(\frac{x}{R^5}\right) = \frac{-y}{3(c^2+x^2)R}$$

Eq. 11